UNIVERSITY OF OKLAHOMA

GRADUATE COLLEGE

SIMULTANEOUS ASSIMILATION OF RADAR AND SATELLITE DATA FOR CONVECTIVE SCALE NWP USING HYBRID ENSEMBLE VARIATIONAL DATA ASSIMILATION APPROACH

A THESIS

SUBMITTED TO THE GRADUATE FACULTY

in partial fulfillment of the requirements for the

Degree of

MASTER OF SCIENCE IN METEOROLOGY

By

SIJIE PAN
Norman, Oklahoma
2017

SIMULTANEOUS ASSIMILATION OF RADAR AND SATELLITE DATA FOR CONVECTIVE SCALE NWP USING HYBRID ENSEMBLE VARIATIONAL DATA ASSIMILATION APPROACH

A THESIS APPROVED FOR THE
SCHOOL OF METEOROLOGY

BY

_____
Dr. Jidong Gao, Chair

_____
Dr. Xuguang Wang, Co-Chair

_____
Dr. Lance M. Leslie

_____
Dr. David J. Stensrud

Acknowledgements

Earning a Master's Degree is not my individual effort. I appreciate the guidance, support and patience of many people. First of all, I must express my very profound gratitude to my parents, Songhai Pan and Hongmei Cui, for their unfailing support and continuous encouragement during the years of my study at University of Oklahoma. I would like to thank my uncle and aunt, Wenqiu Sun and Qiao Cui, for their care and help when I study abroad. This accomplishment would not have been possible without them.

I am especially grateful to my advisor, Dr. Jidong Gao for his teaching, guidance, advice, support and patience in mentoring me through my thesis research over the past three years and in editing my master's thesis.

I thank my co-adviser and advisory committee, Dr. Xuguang Wang, Dr. David J. Stensrud and Lance Leslie for their guidance and helpful comments on my research over the past three years.

I also thank Dr. Thomas A. Jones for his teaching and guidance of observation operator problems and his comments for my journal publication. I would also like to thank Dr. Yunheng Wang for his help in implement of the source code used in this research.

Scientists and staffs of FRDD and my friends in the school of meteorology, Sam Degelia, Bo Huang, Kenzie Krocak, Xu Lu and Yongming Wang, are appreciated for their very valuable discussions with me.

The majority of funding for this research was provided by NSF Grant AGS-1341878 and the NOAA Warn-on-Forecast project. The experiments in this thesis were

performed on the machine constructed by NOAA Research and Development High Performance Computing Program and the OU Supercomputing Center for Education and Research at the University of Oklahoma.

Table of Contents

List of Tables

List of Figures

Abstract

Recently, an ensemble of the three-dimensional variational data assimilation (En3DA) system has been developed based on Advanced Regional Prediction System (ARPS) three-dimensional variational (3DVar) data assimilation (DA) system. However, the DA system is basically designed for radar data assimilation and only compatible with the ARPS model. In this study, the DA system is extended to include the interface that link the DA system with the broadly used Weather Research and Forecasting (WRF) model and to also incorporate additional satellite retrieval data into the DA process. A major goal here is to evaluate whether simultaneous assimilation of satellite retrieval data and radar data through an En3DA approach has positive impacts on initializing and forecasting convective-scale weather.

The first part of this thesis describes the details about the WRF interface and algorithm of assimilating selected satellite data in the En3DA system. To better drive the WRF model, a post-processing program is introduced after DA. The forward operator and its adjoint for satellite data assimilation are embedded into the En3DA system. This DA system and the WRF model are then tested with an idealized tornadic supercell case and a real data tornadic supercell case. More precisely, an idealized supercell storm initialized by the sounding from the tornadic event occurred on 20 May 1977 Del City, Oklahoma, and the real data case is the 26 May 2016 Solomon, Kansas EF-4 tornadic thunderstorm case.

The idealized case evaluates the assimilation of simulated radar and satellite retrieval data under different storm environments. Radar radial velocity, reflectivity, satellite derived cloud water path (CWP) and total precipitable water (TPW) data are

produced from the simulated supercell storm, and then assimilated into the WRF model. Two types of experiments are performed. Radar and satellite CWP data are assimilated firstly under a perfect storm environment. Additional TPW data is assimilated under a dry biased environment in the second type of experiments. The first set of experiments indicates that incorporating satellite CWP data into radar data assimilation leads to a much faster initiation of supercell storms. Assimilating CWP data primarily improves the analyses of non-precipitating hydrometeor variables such as cloud and ice, as well as temperature. Results from the second set of experiments demonstrate the importance of the storm environment. With the biased storm environment, assimilation of CWP and radar data can enhance the analyses, but the forecast skill rapidly decreases in 1-hour forecast. Experiments show that the TPW data has a large effectiveness in the first 30-min free forecast, but gives little impact thereafter. The reason is that the TPW is a vertical integration of water vapor content and cannot provide information of the moisture vertical structure which is the key to the storm development.

A similar experimental design is applied to a tornadic supercell storm event on 25-26 May 2016. Four sets of experiments are performed. The first one does not assimilate any data (NoDA), the second one assimilates CWP data alone (CWP), the third one assimilates radar data alone (RAD), and the final one assimilates both radar and satellite data (RADCWP). It is found that best DA and forecast results are provided in RADCWP experiment. In the DA results, the structures of the supercell storm including cold pool, wind fields and reflectivity pattern are reasonably analyzed in the RADCWP. The scope and intensity of strong precipitation area (indicated by reflectivity field) and cold pool area look more reasonable. The positive impacts of both data types are also

supported by 1 hour free forecasts after DA cycling. Biases and RMS errors are smallest as well as skill scores are best for the RADCWP experiment when both data are used.

In general, the idealized case with inaccurate moisture environment indicates that the correctness of storm environment is a significant component to the accuracy of the convective scale NWP. The combination of radar data and satellite data within the En3DA method results in better analyses and forecasts than that when only using radar data for the idealized. In the real data case, the positive impact of both radar and CWP data is demonstrated. However, this is only one real data case. Further investigations of the influence of radar and CWP data in storm-scale DA and convective NWP, especially the impact of more satellite data and product such as TPW, will be conducted in the future studies.

Chapter 1 Introduction and Motivation

The mission of the NOAA's Warn-on-Forecast (WoF) program is to make more accurate forecasts of high impact weather events such as tornadoes, hailstorms, flash floods, and damaging windstorms in convective scale (Stensrud et al. 2009). To do this, high resolution remote sensing data, such as radar data and satellite data that can resolve the internal storm structures have to be used. Many studies have demonstrated that effective utilization of high resolution remote sensing data in convective scale numerical models leads to significant improvement in severe weather analyses and forecasts (Dowell et al. 2004; Gao and Stensrud 2012; Gao et al. 2004; Johnson and Wang 2016; Johnson et al. 2015; Jones and Stensrud 2012; Jones et al. 2013; Jones et al. 2016; Stensrud and Gao 2010; Wang and Wang 2016; Wheatley et al. 2015; Yussouf et al. 2013).

Radial velocity and reflectivity from the Weather Surveillance Radar-1988 Doppler radar (WSR-88D, Crum et al. 1993) can provide important wind and hydrometeor information over areas of precipitation. Assimilating observations from multiple radars was a primary tool to understand internal structures and dynamics of convective storms during the past 20 years (Aksoy et al. 2009; Dowell et al. 2011; Dowell et al. 2004; Gao and Stensrud 2012; Gao et al. 2004; Sun 2005; Yussouf and Stensrud 2010). For example, Sun et al. (2005) demonstrated the usefulness of radar data in a four dimensional variational (4DVar) system for initializing and forecasting a severe storm. Yussouf and Stensrud (2010) showed the advantages of using the ensemble Kalman filter (EnKF) method to assimilate high temporal frequency radar data for convective storms. Despite some encouraging results, a major shortcoming of

radar data assimilation remains. Only wind and some of the hydrometeor variables are closely related to radar observations, but other model variables are not directly observed. For instance, non-precipitating cloud water and ice which are excluded from commonly used reflectivity operator may not be properly analyzed, especially in a 3DVar system. On the other hand, the environment information such as water vapor content and air temperature etc., cannot be captured by radar network. The problem must be solved because the environment is straightforwardly connected to the moisture and thermodynamic condition of the atmosphere which has large influence on either generation or dissipation of convective storms.

Comparing to the radar data, the employment of satellite data in NWP is very mature at synoptic scale and alpha mesoscale (Harris and Kelly 2001; Matricardi et al. 2004; Saunders et al. 1999; Vukicevic et al. 2006; Weng 2007; Weng and Liu 2003). One popular use of satellite data is the direct assimilation of satellite radiances. By assimilating radiances, uncertainties and discrepancies in the retrieval algorithms which are different between instruments are avoidable (Derber and Wu 1998). However, due to the inaccuracy of Radiative Transfer Models (RTM) and their sensitivity to the channels being assimilated (Migliorini 2012), satellite radiances are generally assimilated over clear-sky areas. Although considerable progress in cloudy radiance assimilation have been reported recently (Okamoto et al. 2014; Pavelin et al. 2008; Polkinghorne and Vukicevic 2011; Polkinghorne et al. 2010; Prates et al. 2014; Stengel et al. 2013; Vukicevic et al. 2004; Weisz et al. 2007), applying their methods introduces additional uncertainties because of different assumptions between the model physics and RTMs, especially at high spatial and temporal resolutions (Zupanski et al. 2011).

The application of satellite data in convective scale NWP has not been extensively explored so far. One such application is to use derived products from satellite observations, such as cloud water path in convective-resolving scale data assimilation and forecast. Jones et al. (2013) used CWP retrievals from the Geostationary Operational Environmental Satellite (GOES) to improve hydrometeors content over cloudy area for the severe weather event occurred on 10 May 2010. In the experiments, both radar data and CWP data were assimilated using the WRF Data Assimilation Research Testbed (DART) program (Anderson et al. 2009) with 40 ensemble members. Results demonstrated that a better structure of the storm with elimination of spurious cells was produced by assimilating CWP data at 15-min intervals over a 3-h DA period compared to the experiments without CWP assimilation.

With the launch of GOES-16 (Nov. 19, 2016), formally known as GOES-R, the application of high resolution satellite data in convective NWP will be expected to grow rapidly. Both WSR-88D radar observations and GOES-16 satellite products contain useful information about internal storm structures. In addition, GOES-16 products, such as TPW data contain water vapor information, which is one of the most important components of the storm environment.

The environmental conditions that surround convection can be as important as the convection itself and is beneficial to create a good initial condition for severe weather forecasting. Kuo et. al (1996) established a set of experiments indicating that even for a first guess with a very poor initial moisture field, 4DVar was quite effective in improving moisture distribution after precipitable water is assimilated. But his study was only for mesoscale. For convective scale NWP, the importance of the storm

moisture environment has not been extensively studied. So in this paper, we study the impact of CWP and TPW (both of will be GOES-16 products) on the analysis and forecast of an idealized supercell storm together with radar data using the En3DA method (Gao et al. 2016).

A concept of the ensemble of DAs (EDA) used by Meteo France and ECMWF (Berre et al. 2007; Bonavita et al. 2012) was adopted in Gao et al. (2016). The only difference is that the extended control variables or so-called alpha control variable (Lorenc 2003; Wang et al. 2008) was used for introducing ensemble covariances into the variational system. The EDA approach would be very expensive if the core DA scheme is 4DVar. But En3DA uses 3DVar as its core DA scheme which takes the advantages of both ensemble assimilation technique and 3DVar. First of all, the flow-dependent background error covariances estimated from ensemble forecast are allowed in an EDA scheme. Furthermore, multivariate correlations are more conveniently modeled by ensemble covariances. Finally, the computationally high efficiency of 3DVar method is retained even if the flow-dependent covariances have been introduced. The alpha control variable method was used in early studies for direct assimilation of simulated or real radar data for convective scales (Gao and Stensrud 2014; Wang and Wang 2016). However, it has not been used for assimilating satellite data for convective scale NWP. The En3DA was developed for Advanced Regional Prediction System (ARPS, Xue et al. 2000; Xue et al. 2003; Xue et al. 2001). In this study, we first develop an interface which links En3DA with WRF model and diagnoses unanalyzed variables through minimization progress which are prognostic variables in WRF model. Then the DA system is used to perform a set of OSSEs and a set of real-data

experiments. For the idealized case, first of all, radar data and satellite CWP data are assimilated under the perfect storm environment, similar to Jones et al. (2013), but under this En3DA framework. Furthermore, additional TPW data is assimilated under the storm environment with dry bias in the environment. The motivation here is to further examine to what extent the recently launched GOES-16 produced CWP and TPW can benefit convective scale data assimilation and NWP in addition to radar data. A case of tornadic thunderstorm occurred on 25-26 May 2016 is also performed to investigate how the CWP data improve the storm-scale DA and convective NWP.

The remaining structure of this paper is as follows. The methodologies of En3DA scheme, forward operator of radar and satellite data and verification approach are briefly described in chapter 2, while chapter 3 provides details of the OSSEs, including experimental design, analysis results and forecast evaluation. Chapter 4 further discusses the impact of satellite retrieval data in real data case. Conclusions are given in section 5.

Chapter 2 Methodology

2.1 Data Assimilation Algorithm

In the following section, we briefly describe the En3DA method (Gao et al. 2016) adopted in this study. Assume we have the basic concept of En3DA method is to minimize cost function J_k with respect to the control variables, where k is the number of ensemble members. The cost function J_k can be defined as the background term and the observation term plus other constraint terms:

$$J_k = \frac{1}{2}\left(\mathbf{x}_k - \mathbf{x}_k^{\boldsymbol{b}}\right)^T \mathbf{B}^{-1}\left(\mathbf{x}_k - \mathbf{x}_k^{\boldsymbol{b}}\right) + \frac{1}{2}[H(\mathbf{x}_k) - y_k^o]^T \mathbf{R}^{-1}[H(\mathbf{x}_k) - y_k^o] + J_c(\mathbf{x}_k) \tag{2.1}$$

where $\mathbf{x}_k$ and $\mathbf{x}_k^b$ are the analysis and background state vectors for ensemble member k; $H(\mathbf{x})$ is the observation operator; y_k^o are the observation vectors. Similar to the stochastic EnKF (Houtekamer and Mitchell 1998), random perturbations are applied to the original observation to generate various observations for each ensemble member. The constraint term J_c could contain any dynamic equation as a strong or weak constraint. We assume that the model dynamics are biased and corrections are allowed, thus the mass continuity equation is introduced into the penalty term J_c as a weak constraint. Details relating to this constraint term were discussed by Gao et al. (2016). **B** and **R** are the background and observation error covariance matrices respectively. Following Derber and Rosati (1989) and Courtier (1997), define an alternative control variable **v** that makes optimal analysis increment $\Delta\mathbf{x}_k = \mathbf{B}_e^{1/2}\mathbf{v}_k = \left(\mathbf{x}_k - \mathbf{x}_k^b\right)$ Then the cost function can be written in a preconditioned incremental form

$$J_k = \frac{1}{2}\mathbf{v}_k^{\mathrm{T}}\mathbf{v}_k + \frac{1}{2}\left[H\left(\mathbf{x}_k^b + \mathbf{B}_e^{1/2}\mathbf{v}_k\right) - y_k^o\right]^{\mathrm{T}}\mathbf{R}^{-1}\left[H\left(\mathbf{x}_k^b + \mathbf{B}_e^{1/2}\mathbf{v}_k\right) - y_k^o\right] + J_c(\mathbf{v}_k). \tag{2.2}$$

The observation error covariance **R** includes instrument errors, representativeness errors and errors in the observation operator (Lorenc 1986; Kalney 2003). The observation error correlations may exist in particular circumstances, such as the observations are collected by the same platform, observations are more dense than the model spatial resolution or errors contain in the forward operator. However, they are difficult to estimate. Therefore, serval efforts are made to minimized the correlations, such as thinning dense observations to generate so-called super-obs and improving observation operators to be as accurate as possible. Then observation errors are assumed to be independent and uncorrelated so that the observation error covariance is a diagonal matrix (Gao et al. 2004).

The background error covariance **B** is the most important component in DA. Information from observations are spread across the whole domain according to the structure of the background error covariance. In another word, the correlation in spatial and the cross-correlation between different variables are determined by the background error covariance. In fact, however, we never know the exact errors between the model forecast and the true state of the atmosphere. For the traditional 3DVar, a static, homogeneous and isotropic error covariance matrix is commonly used which means the background errors do not change in time, and it cannot reflect the real state of the model forecast errors. Therefore, to more accurately estimate background error covariance is an important problem to DA process. An essential difference of En3DA from the 3DVar framework is that the flow-dependent covariance $\mathbf{B_e}$ is derived from an ensemble of

forecasts and establishes correlations between different model variables. A similar formula was also proposed in Lorenc (2003), Buehner (2005) and Wang et al. (2008), Wang (2010).

In our experiments, an ensemble of En3DA analyses and an extra control member were performed simultaneously by minimizing the cost function (2) to update the analysis variables. The ensemble covariance used in En3DA analysis for each ensemble member is derived from other ensemble forecasts except itself. For the control member, the covariance is estimated from the entire ensemble forecasts. Then the ensemble analyses were centered on the control analysis and inflated using the statistical information from the ensemble backgrounds and analyses. The inflation process is applied on each grid point according to the equation

$$\mathbf{x}_k^{\boldsymbol{a}} = \mathbf{x}_c^{\boldsymbol{a}} + \gamma(\mathbf{x}_k^{\boldsymbol{a}} - \overline{\mathbf{x}^a}) + (1 - \gamma)(\mathbf{x}_k^{\boldsymbol{b}} - \overline{\mathbf{x}^b}), \tag{2.3}$$

where $\mathbf{x}_c^a$ is the analysis of the control member, $\mathbf{x}_k^a - \overline{\mathbf{x}^a}$ indicates the perturbation from the mean of ensemble analyses, and $\mathbf{x}_k^b - \overline{\mathbf{x}^b}$ denotes the perturbation with respect to the mean of ensemble background forecasts. The γ is set to 0.5 in this case such that the new analysis perturbations are calculated by mixing half of analysis and half of original background perturbations. Similar approach was proposed for EnKF in Zhang et al. (2004) and Whitaker and Hamill (2012). The ensemble analyses after inflation can be considered as the initial conditions for the next step. Once the control analysis and the initial conditions of ensemble members are prepared, 5-minutes forecasts are started and then a DA cycle is finished. The above operations are repeated for several times that depend on the number of DA cycles.

Closely following Gao et al. (2013) and Gao and Stensrud (2014), both radial velocity and reflectivity are always assimilated in this study. The CWP and TPW data are incorporated in the DA process to evaluate the impact of these satellite derived data. The forward operators for radial velocity and reflectivity are chosen from Gao and Stensrud (2012). Work by Chen et al. (2015) is adopted for converting model variables to CWP. For computing TPW, a derivation defined by the theoretical basis document for GOES-16 Advanced Baseline Imager (Minnis et al.) is used in our analysis system. Forward operators introduced here are briefly discussed in next section. Due to the unavailability of TPW data from GOES-16 until now, only CWP data from GOES-13 is used as satellite retrieval data in real data case.

2.2 WRF Interface

Control variables in the En3DA system include the three-dimensional wind field u, v and w; potential temperature θ; air pressure p; water vapor mixing ratio q_v and hydrometeors that depends on microphysics scheme, usually containing cloud water mixing ratio q_c, rain water mixing ratio q_r, ice mixing ratio q_i, snow mixing ratio q_s, and graupel mixing ratio q_g. However, the WRF model requires geopotential ϕ and mass of dry air μ instead of pressure p as prognostic variables. To better initialize the WRF model, another post-process is applied after minimization process to recalculate the geopotential and dry air mass so that the updated variables exactly match the prognostic variable of the WRF model. The increment of the dry air mass in column can be written as:

$$\mu'_a = \frac{p'_{sfc} - (\mu + \mu') \times \int_0^{1.0} q'_k d\eta_w}{1 + \int_0^{1.0} q_k d\eta_w} \tag{2.4}$$

where p'_{sfc} is the analysis increment of surface pressure; μ is the base state of dry air mass in column from the background forecast; μ′ is the perturbation of the background dry air mass in column; q'_k represents the analysis increment of the mixing ratio of the water vapor; q_k is the mixing ratio of the water vapor obtained from the background; and η_w indicates the vertical coordinates. Once the increment of the dry air mass is obtained, the geopotential height at a particular model level k+1 can be computed by using the air density and dry air mass as follows:

$$\phi'_{k+1} = \phi'_k + \int_k^{k+1} \left(\frac{\mu'_a}{\rho_k} + (\mu + \mu') \times \frac{\rho'_k}{\rho_k^2} \right) d\eta_w \tag{2.5}$$

where ρ_k is the air density at k^{th} model level; ρ'_k is the increment of air density at the same level. Otherwise, the symbols are similar to the increment calculation of the dry

air mass. It is worth noting that the first level of the geopotential height represents the terrain.

2.3 Observation Operator

2.3.1 Forward Operator of Radar Observations

The operational radars choose Volume Coverage Patterns (VCPs) based on the type of weather occurring. Corresponding to the operational WSR-88D scanning strategy, radial velocity and reflectivity are calculated on 14 different elevation angles for deep convection mode. Available radar observations are located on model grid points.

The observation operator of radial velocity is defined as the following equation

$$V_r = u \sin \phi \cos \mu + v \cos \phi \cos \mu + (w - w_t) \sin \mu \tag{2.6}$$

where $(\mathrm{u}, \mathrm{v}, \mathrm{w})$ are the wind components from the model forecast on staggered grid points, w_t is the terminal velocity of precipitation on the same grid, ϕ is the azimuthal angle of radar beam and μ is the elevation angle considering the effect of the curvature of the Earth.

The forward model for calculating reflectivity is based on Smith et al. (1975) and Ferrier (1994). Same as Gao et al. (2012), radar reflectivity factor is obtained by gathering the rain water, snow and graupel mixing ratio:

$$Z_e = Z(q_r) + Z(q_s) + Z(q_g), \tag{2.7}$$

$$Z_{dB} = 10 \log_{10} Z_e. \tag{2.8}$$

Introducing three types of hydrometeor variables into the reflectivity forward operator may lead to underestimation of DA solution since the number of unknown variables is more than that is already known. Background temperature from NWP model is taken into account for determining the hydrometeor variables from the reflectivity.

2.3.2 Forward Operator of Satellite Observations

Satellite data is a major resource for storm-scale data assimilation. It has a wider spatial coverage than radar and fulfills deficiencies of radar observations. Two types of satellite retrieval data are prepared for this study. CWP is the column amount of liquid and frozen water (in kg m^{-2}) in the cloud. It represents the horizontal distribution and weight of the liquid and ice hydrometeors in the atmosphere. For the clear sky, the CWPs are 0 kg m^{-2}. No matter the concentration of liquid water or ice in clouds goes up, so does the value of CWP. For the reason that CWP is a value of vertical integration, it cannot illustrate the vertical distribution of cloud water. However, information provided by CWP is still helpful to improve the analysis of the non-precipitating hydrometeor variables that cannot be obtained from the reflectivity observation. Besides CWP, cloud base heights, cloud top heights and cloud phases are additionally offered in real time retrieval algorithm (Minnis et al. 2008a; Minnis et al. 2008b; Minnis et al. 2011).

CWPs are created by integrating hydrometeor variables from the background in atmospheric columns for calculating differences to the observation in cost function. First, the cloud water mixing ratio and ice mixing ratio are summed to compute the total cloud water mixing ratio on each grid point. Then the CWP is obtained by accumulating the total water mixing ratio from the cloud base to top following the formula:

$$\mathrm{CWP} = \frac{1}{g}\int_{CBP}^{CTP} [q_c(p) + q_i(p)]dp \tag{2.9}$$

Where q_c and q_i are the cloud water and ice mixing ratio, g is the gravity acceleration, p is the air pressure on the model level, CBP and CTP represent the cloud base pressure and cloud top pressure, respectively. Cloud base pressure is chosen by finding the lifted

condensation level (LCL) and cloud top pressure is defined by locating the pressure where the liquid water and ice mixing ratio are less than 10^{-3} g kg^{-1}. Observed CWP includes the contribution from precipitating hydrometeors (qrain, qsnow etc).

TPW is another type of satellite retrieval. It recounts the amount of liquid water (in cm) if all the atmospheric water vapor in the column was condensed. In spite of also a value of vertical integration, water vapor mixing ratio is possible to be adjusted by TPW directly rather than by using the ensemble covariances with other data. To keep the consistency between the forward operator of TPW and the method for GOES-R ABI (Li et al. 2010), only water vapor between surface and 300 hPa is accumulated to derive TPW due to rare water vapor content above 300 hPa. The algorithm defined in GOES-16 ABI document is used as TPW forward operator. Only water vapor mixing ratio is required:

$$\text{TPW} = \frac{1}{\rho_w g}\int_{p_s}^{300hPa} q_v\,(p)dp. \qquad (2.10)$$

In this equation, ρ_w equals to 1000 kg m^{-3} which indicates the water density, p_s is the surface pressure in hPa, and q_v is the water vapor mixing ratio. Otherwise, the calculation is similar to that used for CWP.

2.4 Methods Used to Verify the Results

To access the impact of assimilating the radar and satellite observations, several graphical and statistical methods are used to provide great objective information from the different parameters than the subjective evaluation of critical characteristics of storms such as reflectivity core, low-level cold pool and mid-level warm core etc. Beside the traditional statistics in the form of bias and root-mean-square error (RMSE), a set of statistical estimates of skill, the Probability of Detection (POD), False Alarm Rate (FAR), Critical Success Index (CSI) and Heidke Skill Score (HSS), is used to make up for determining whether or not the radar and satellite data has the ability to improve the severe thunderstorm forecast. These statistics are plotted for visualization to better represent the results.

Bias and RMSE are widely used as statistical method. They are usually calculated by comparing the simulated observation taken from backgrounds and analyses against the truth observation as shown in following equations:

$$Bias = \frac{1}{N}\sum_{n=1}^{N} y_n^o - H(\mathbf{x}) \tag{2.11}$$

$$RMSE = \sqrt{\frac{\sum_{n=1}^{N}[y_n^o - H(\mathbf{x})]^2}{N}} \tag{2.12}$$

where N is the number of selected true observations.

Skill scores introduced above are the commonly used measurement in the research community. To calculate these skill scores, contingency tables have to be constructed by 4 components: Hits, Misses, False Alarms (FAs) and Null Forecasts (NFs). In our experiments, a threshold of 40 dBZ for reflectivity is used as criteria for all skill scores.

For instance, if an experiment generates reflectivity value greater than 40 dBZ on grid point which in the truth simulation the reflectivity value is greater than 40 dBZ, then this is considered a "hit". In contrast, the reflectivity less than 40 dBZ in an experiment with the threshold is observed in the reference truth is considered a miss detection. Furthermore, if the reflectivity greater than 40 dBZ are produced in an experiment while the criterion is not exceeded in truth simulation, then it is considered a false alarm. And if the threshold is not surpassed by either the experiments or the truth simulation, the forecast is considered a correct null forecast. An example contingency table is shown in Table 1. The skill scores can be calculated once the 4 elements are separated into the contingency table:

$$POD = \frac{a}{a+c} \tag{2.13}$$

$$FAR = \frac{b}{a+b} \tag{2.14}$$

$$CSI = \frac{a}{a+b+c} \tag{2.15}$$

$$HSS = \frac{2(ad-bc)}{(a+c)(c+d)+(a+b)(b+d)} \tag{2.16}$$

where a, b, c, and d are hits, false alarms, misses, and null forecasts separately.

TABLE 1. Contingency table for calculating skill scores.

Contingency Table		Event Observed	
		Yes	No
Event Forecast	Yes	a (Hits)	b (FAs)
	No	c (Misses)	d (NFs)

We can see that the POD and CSI grows with increasing of hits and FAR grows with increasing of b. However, these three scores only reflect one-side of quality of the forecasts. A good forecast should maximize the number of "hits" leading to a high POD with low FAR as a consequence of suppressing false alarms. The accuracy of the forecasts can be better represented by a more complicated parameter HSS which takes all components of contingency table into account. Because $a+b$, $a+c$, $b+d$ and $c+d$ are consistent which are obtained from the forecast and observation, from equation 2.16, it can be readily seen that when FAs and misses are 0, then HSS equals 1 which indicates a perfect forecast. In the contrast, if FAs and misses are 1, then HSS equals -1, suggesting that the forecast is totally wrong. And finally, if hits and FAs are both 0, then HSS is 0 and considered as no-skill forecast. Therefore, the range of HSS is from -1 to 1, but only positive HSS represents a valid forecast.

Chapter 3 Observing System Simulation Experiment

3.1 Model Configuration and Truth Simulation for OSSE

To test the En3DA approach briefly discussed above, a fully compressible, non-hydrostatic Advanced Research Weather Research and Forecasting (WRF-ARW) model version 3.6.1 was used in a three-dimensional idealized mode for quarter circle shear supercell simulation. The horizontal spatial resolution is 1 km with 80 points in north-south and east-west direction, and a stretched 40 eta levels in vertical up to 20km above ground level (20km AGL, approximate 50hPa) was taken so that the distance between each level has a nearly constant value from low-altitude towards to the model top. Open lateral boundary conditions and Rayleigh damping for the top boundaries were used for this idealized case. The length of simulation is up to 2 hours.

The simulation was initialized by a slightly modified sounding (Fig. 1, black line) of a classic supercell event occurred on 20 May 1977 Del City, Oklahoma. Similar to the past studies (Adlerman and Droegemeier 2002; Noda and Niino 2003; Rotunno and Klemp 1985; Weisman and Klemp 1982), an ellipsoidal thermal bubble was added in truth simulations to trigger the convection. The warm bubble had potential temperature perturbation of 3K at the location $x = 60$ km, $y = 25$ km, $z = 1.5$ km with 10 km horizontal radius and 1.5 km vertical radius. The single-moment Thompson scheme, a five hydrometeor classes scheme containing predicted number concentration of ice and rain was used to depict the microphysics process. The turbulence parameterization scheme was the standard 1.5-orer TKE closure. Cloud and radiation physics was not applied in idealized simulation.

During the truth simulation, the initial convection intensifies in the first 30 min (Figure 2a-d) accompanied by cloud forming around 10 min (Figure 3a). Rain water appears at 15 min (Figure 3b), while ice phased hydrometeors are generated at 20 min (Figure 3c-e). The storm keeps developing and reaches strongest intensity at 40 min (Figure 2e-f), then starts to split (Figure 2g) with a little intensity decreasing simultaneously. A typical behavior of supercell thunderstorm is generated since 40 min. The right-splitting cell (which stays at the center of the domain) tends to control the system after this point indicated by warm core in the mid-troposphere, cold pool near the surface, classical characteristic "hook echo" and updraft reaching a maximum value 64 $m\ s^{-1}$ around 10km AGL at 75 min.

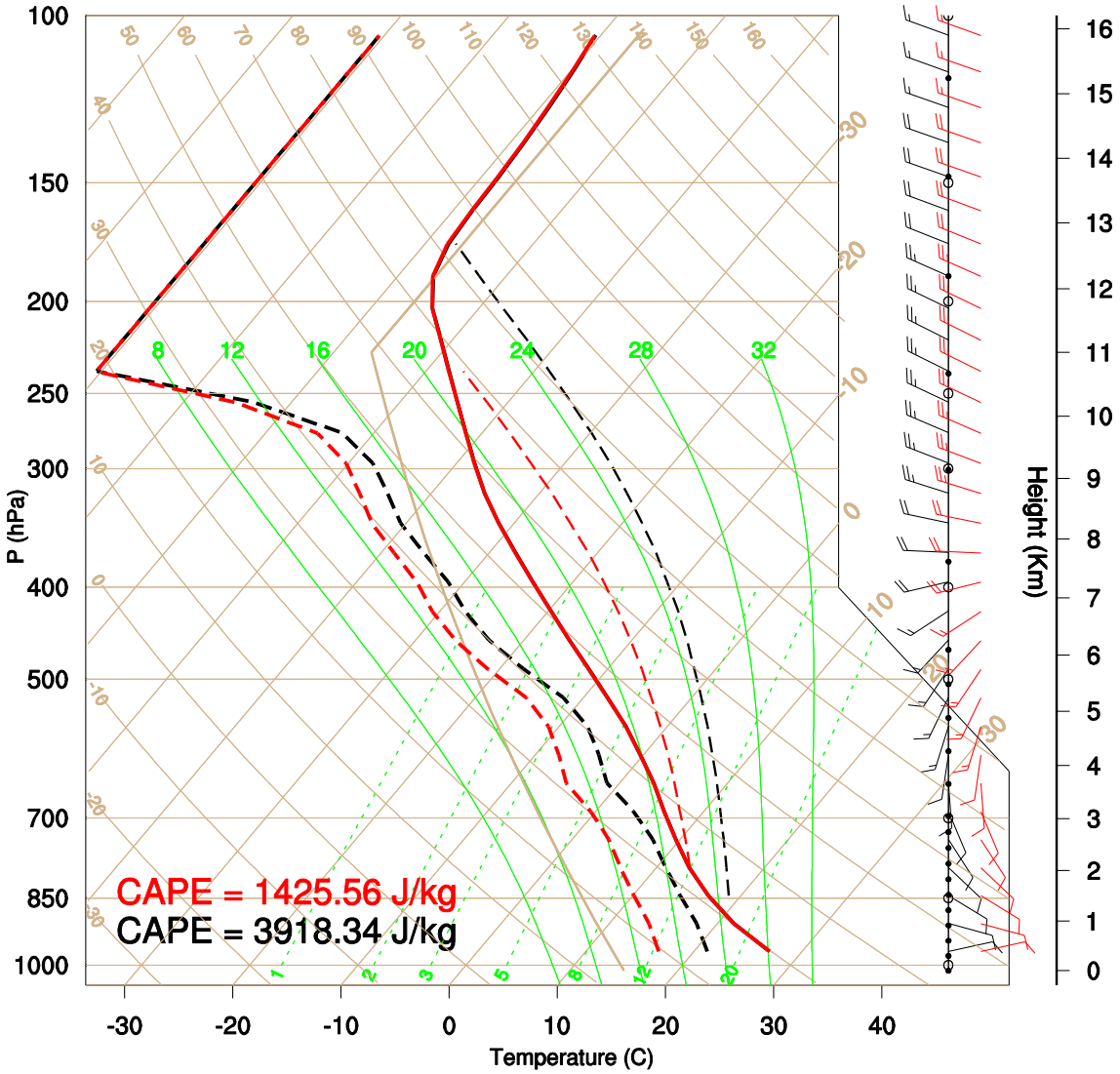

Figure 1. Slightly modified sounding of a classic supercell event occurred on 20 May 1977 Del City, Oklahoma for the truth simulation (black), first set of experiments (black) and second set of experiments (red) including temperature (solid line); dew point temperature (thick dashed line); and CAPE (thin dashed line).

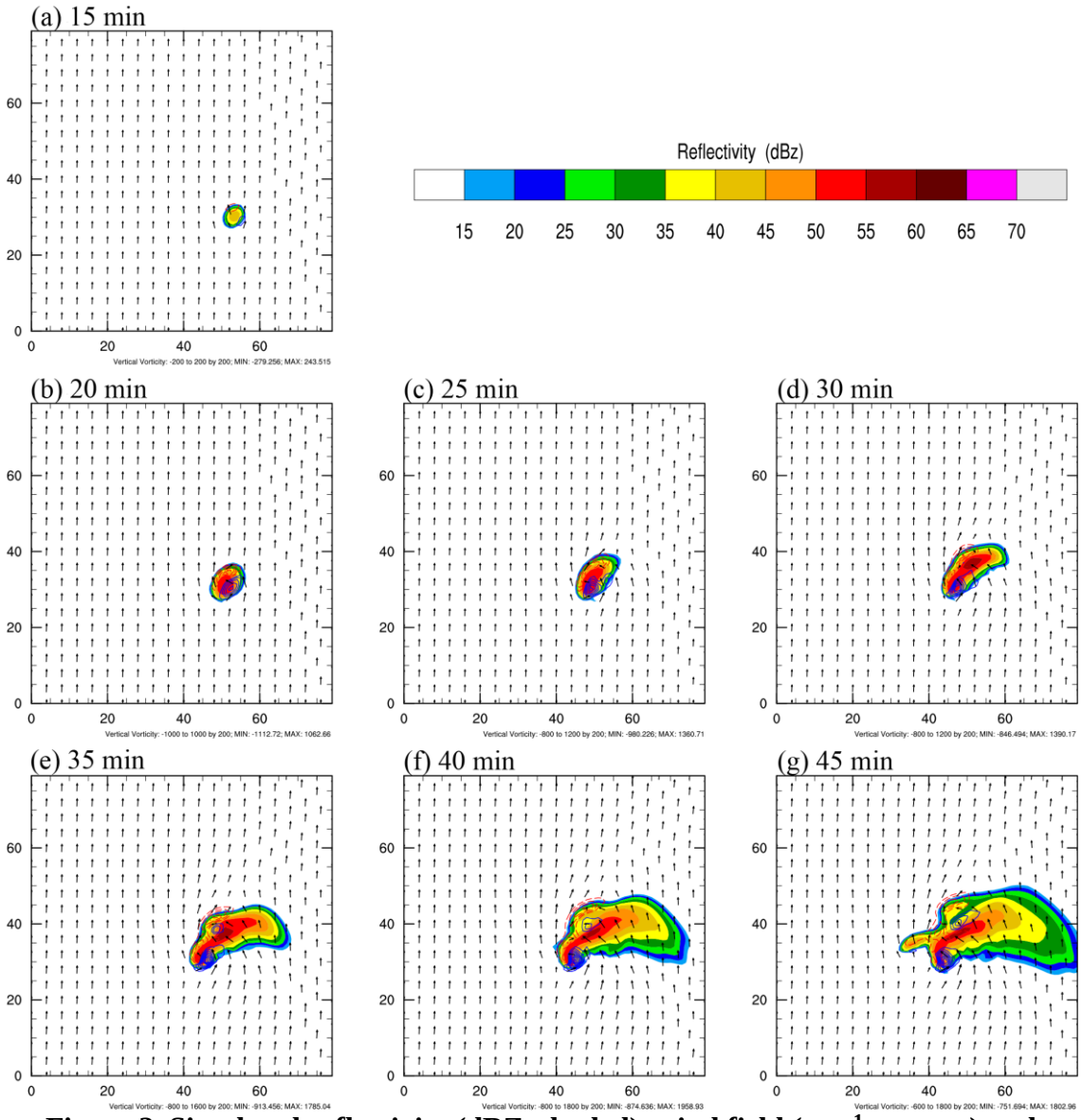

Figure 2. Simulated reflectivity (dBZ, shaded), wind field (m s^{-1}, arrows) and relative vorticity (10-5 s^{-1}, contours) at 4 km AGL from 15 min to 45 min as reference truth. Blue solid lines represent positive vorticities and red dashed lines are negative vorticities.

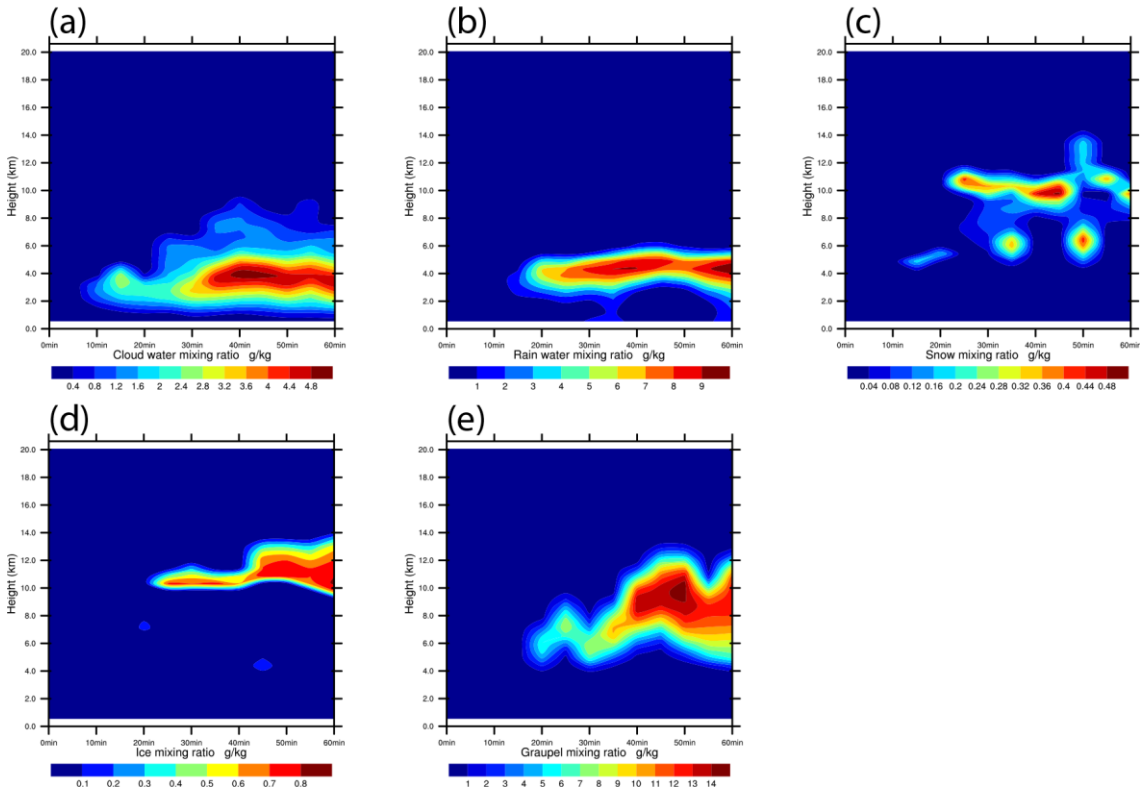

Figure 3. Time-Height composites of maximum hydrometeor mixing ratios (g kg^{-1}) for truth simulation. (a) Cloud water; (b) Rain water; (c) Snow; (d) Ice; and (e) Graupel.

3.2 Experimental Design

As shown in Table 2, we performed two sets of experiments with backgrounds started from different soundings. Both go through the same procedure to examine the impact of various data. The first set of DA experiments is initialized using the sounding same as that in the truth simulation, but without introducing an ellipsoidal thermal bubble (so without assimilating radar and satellite data, the storm will never develop). The second set of experiments uses a sounding with dry bias (red line in Figure 1) to define storm environment. In both experiments, ensemble size is set to 50. To generate initial ensemble members, random perturbations are added to the horizontally homogeneous backgrounds for both experimental groups. The random perturbation has a normal distribution with zero mean and a standard error of 5 m s^{-1} for horizontal wind, 3 m s^{-1} for vertical wind and 3 K for potential temperature. Symmetrical three-dimensional smoothing is applied to the perturbations. The method is closely follows Gao and Stensrud (2014). Perturbations are added over the whole domain except 5 points from boundaries which may result in numerical instability near boundaries. No perturbations for hydrometeor, mass of dry air or geopotential are included at the initial time. A 15-min ensemble forecast is launched thereafter so that the random perturbations dynamically grows, leading to a larger ensemble spread that characterizing a more reasonable covariance structure than perturbing the initial sounding randomly only.

The simulated radar and satellite data is sampled from the truth simulation to perform rapid changes of the storm because of occurrence of strong horizontal and vertical variations in it. Random perturbations are also added to simulated radar and

satellite observations for all members except the control one. Normally distributed errors with zero mean and a standard deviation of 1 m s^{-1} are combined with observed radial velocity on each available grid point. For reflectivity, the perturbations which have a Gaussian distribution with zero mean and a standard deviation of 4 dBZ are added to simulated reflectivity observation where the value is greater than the threshold 15 dBZ. The perturbation of CWP has zero mean and 0.2 kg kg^{-1} standard deviation. And random noise for TPW is drawn from a normal distribution with zero mean and 0.4 cm standard deviation. The same set of observation perturbations is used in all experiments.

TABLE 2. Assimilation experiments with different types of each sounding.

	Sounding	Experiment	Radial Velocity + Reflectivity	CWP	TPW
Set 1	Original (black line)	RAD1	√	×	×
		RADCWP1	√	√	×
Set 2	Dry Sounding (red line)	RAD2	√	×	×
		RADCWP2	√	√	×
		RADSAT	√	√	√

In both groups of experiments, satellite data are assimilated 15 minutes prior to assimilate radar data at 5-min interval considering that the non-precipitating cloud could already be generated at that time. Radar data with or without satellite data are assimilated every 5 minutes for a 30-min assimilation-forecast cycle, since at 30 minutes of model integration, the storm develops well in truth simulation (Fig. 4). In all experiments, the correlation scale is 4 km in horizontal and 1 km in vertical for the first outer loop as well as 2 km in horizontal and 1 km in vertical for the second outer loop.

The RAD1 and RAD2 experiments only assimilate radial velocity and reflectivity, identifying the performance of radar DA under different situation of the atmosphere. The RADCWP1 and RADCWP2 experiments bring the CWP data into the radar DA. The final RADSAT experiments combines radar and all satellite data to determine if the TPW data has a positive impact under the dry biased storm environment compared to use radar data or CWP data only. Jones et al. (2015) has demonstrated the effectiveness of clear sky CWP observations on suppressing spurious cells. In our experiments, both zero reflectivity and clear sky CWP are assimilated to inhibit the development of spurious convections in all experiments.

After the 30 minutes assimilation of radar data (or 45 minutes of satellite data assimilation if applied), a 1-hour free forecast is launched with the control member and the results are compared to the truth simulation to evaluate the forecast performance (Fig. 4).

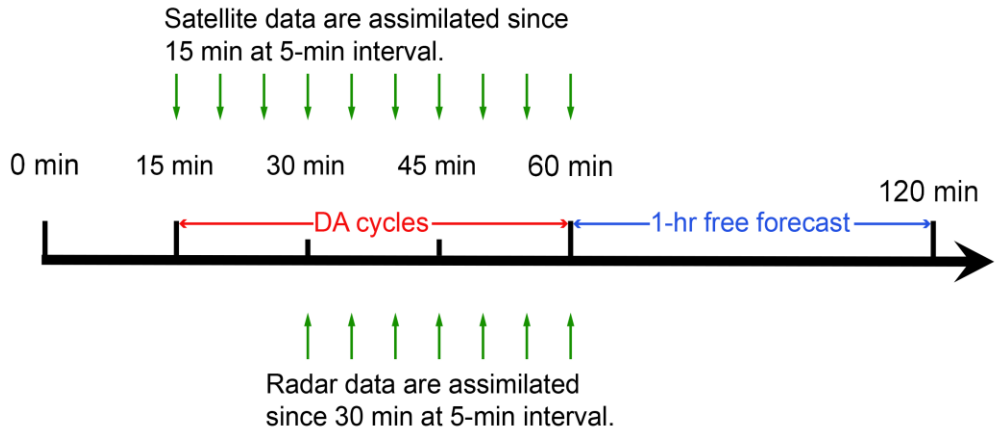

Figure 4. Time series flowchart of radar and satellite data assimilation cycles for experiments listed in Tab. 1.

3.3 The Experiments with Original Sounding

3.3.1 The Diagnostics of Analyses

To inspect the performance of the DA results, the analyses of the control member are plotted for each experiment after 7 DA cycles of radar data, and 10 cycles of CWP data if they are assimilated (at 60 min of model time). Comparing the horizontal winds, vorticities, and reflectivities of En3DA analysis with those of the truth simulation in Figure 5a, both RAD1 (Fig. 5c) and RADCWP1 (Fig. 5e) fairly recover most of the storm characteristics, such as strong reflectivity core, mid-level mesocyclone. Almost all areas of > 50dBZ reflectivity within the right-splitting storm are well recovered in the analysis (Fig. 5e). Two very small spurious perturbations with reflectivity ~ 25dBZ near two major cells are suppressed by assimilating CWP data. The vorticity field indicates that incorporating CWP data improves the dynamic structure of the storm. Stronger directional wind shear near the supercells are shown in RADCWP1 with maximum vorticity 1431 × 10-5 s-1 (Fig. 5e) which is closer to 1640 × 10-5 s-1 in reference truth (Fig. 5a).

Vertical cross sections of reflectivity are created for the truth run and each experiment along y = 35km, the location of the maximum vertical velocity in truth to review the right-splitting storm. The vertical structures of the storm tell more stories. The plots of reflectivity and wind vectors for both experiments basically match the truth simulation (Fig. 5b). However, the patterns of reflectivity and vorticity shown in the cross section for RADCWP1 (Fig. 5f) represent the true state of the atmosphere better, especially near the tropopause (about 10km). The magnitude and vertical vorticity are properly restored in RADCWP1. In comparison with the experiment RAD1 (Fig. 5d),

we can easily see that the analysis results are much improved if CWP data are assimilated (Fig. 5f). Spurious echoes in low- and mid-levels around the major cell are also effectively eliminated.

Temperature fields on mid-troposphere (500hpa) and near the surface (900hPa) are displayed in Fig. 6 for the truth simulation accompanied with RAD1 and RADCWP1 experiments. The RAD1 experiment fails to generate clear low level cold pool of two separate supercells associated with much weaker warm core in the mid-troposphere (Fig. 6c, d). While the RADCWP1 experiment generates more reasonable representations of the low-level cold pool and mid-level warm core simultaneously in the analysis (Fig. 6e, f vs Fig. 6a, b).

Fig. 7 supplies some useful information about vertical distribution of hydrometeor mixing ratios through maximum vertical velocity within the truth simulation. A narrow column of rain water mixing ratio (Fig. 7a) can be found from the surface to 6km with maximum value of > 10 g kg-1 around 5 km in truth simulation. In addition, a large area of snow and ice mixing ratio (Fig. 7b, e) existing between 8 km and 14 km extends to the east boundary of the domain which is the evidence of the cirrus outflow also shown in Figure 5b. The truth run creates a wide column of graupel mixing ratio (Fig. 7c) that is up to 11 g kg-1 from 8 km and 12 km where is collocated with > 2.8 g kg-1 cloud water mixing ratio (Fig. 7d) near 3 km AGL. Each experiment in the first group generates broadly similar properties of clouds to those in the truth, but also reveals some remarkable detail differences. All experiments more or less decrease the maximum concentrations of precipitating cloud water (rain, snow, graupel; Fig. 7f-h, k-m) while the grade of decreasing is much smaller in RADCWP1, indicating that

containing CWP data in En3DA provides enhancement in performance of precipitating cloud water. Furthermore, without assimilated CWP data, non-precipitating hydrometeors (cloud water and ice, Fig. 7i-j) are noticeable less than those in reference truth. The mixing ratio of cloud water analyzed in RADCWP1 is > 2.2 g kg-1 associating with > 0.7 g kg-1 ice mixing ratio that is much closer to the truth run than the experiment assimilating only radar data. The coverage of cloud water > 1.6 g kg-1 and cloud ice > 0.5 g kg-1 in RADCWP1 is comparable to the truth. Result from hydrometeor analysis shows that assimilating CWP data accelerates the initialization of both precipitating and non-precipitating hydrometeor variables.

The evolution of root mean square (rms) errors during the DA assimilation cycles with and without CWP data in En3DA analysis are shown in Figure 8. Within the first 10 min of DA cycles (15 min – 25 min), assimilating only CWP data increases rms error of wind field including u (Fig. 8a), v (not shown), w (Fig. 8b), potential temperature (Fig. 8c) and simulated reflectivity (Fig. 8d) because CWP data does not have enough information to initialize the convection in a short period. After steep increasing, rms error goes down with the cycle moving forward. Once the radial velocity and reflectivity are also assimilated within DA process at later time, the rms errors of all fields are rapidly decreased from 30 min to 40 min and smaller than those assimilating only radar data by at least a factor of 3. Lower and steady rms errors for all variables suggest that the supercell is completely and correctly initialized with radar and CWP assimilation at the end of DA (t=60 min). The errors in the horizontal wind field are around 1 m s-1 in RADCWP1 which is apparently smaller than 3 m s-1 in RAD1. The errors for potential

temperature as well as simulated reflectivity are also significantly reduced by assimilating CWP.

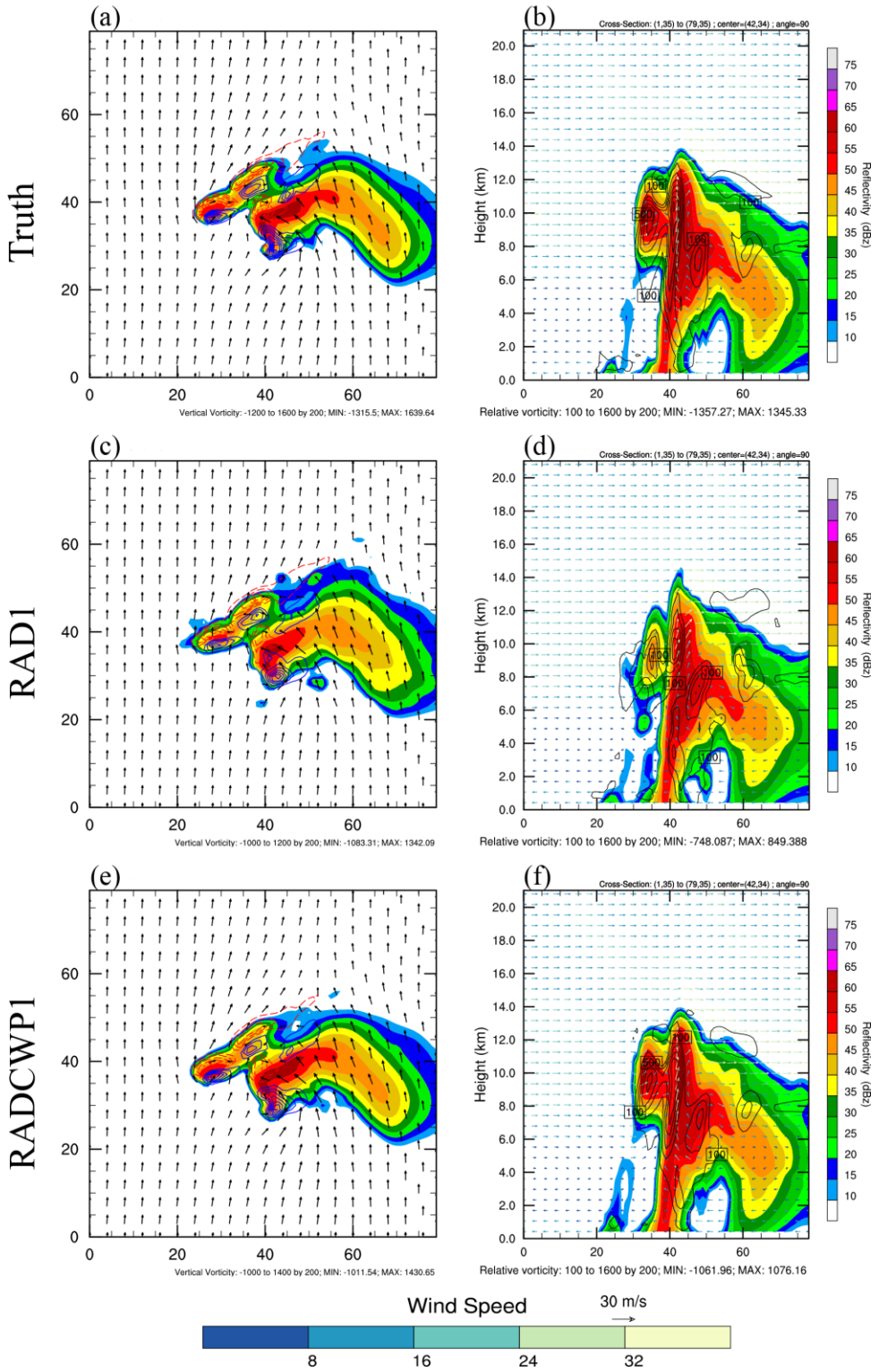

Figure 5. Wind vectors, reflectivity and vorticity in horizontal cross section at 4km AGL (a, c, e) and vertical cross section at y = 35km (b, d, f) for truth simulation, RAD1 and RADCWP1 at 60 min.

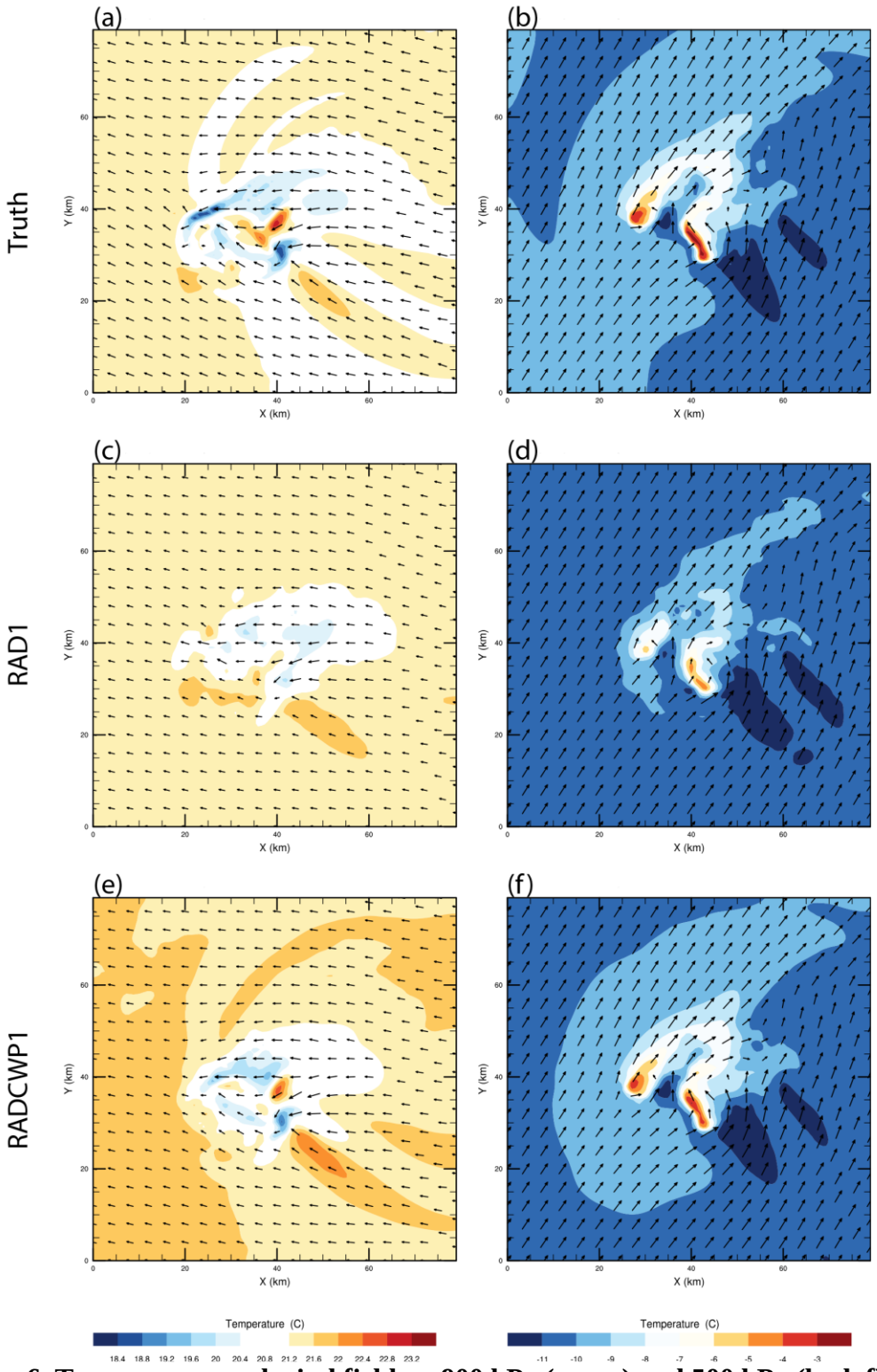

Figure 6. Temperature and wind field on 900 hPa (a, c, e) and 500 hPa (b, d, f) for truth simulation, RAD1 and RADCWP1.

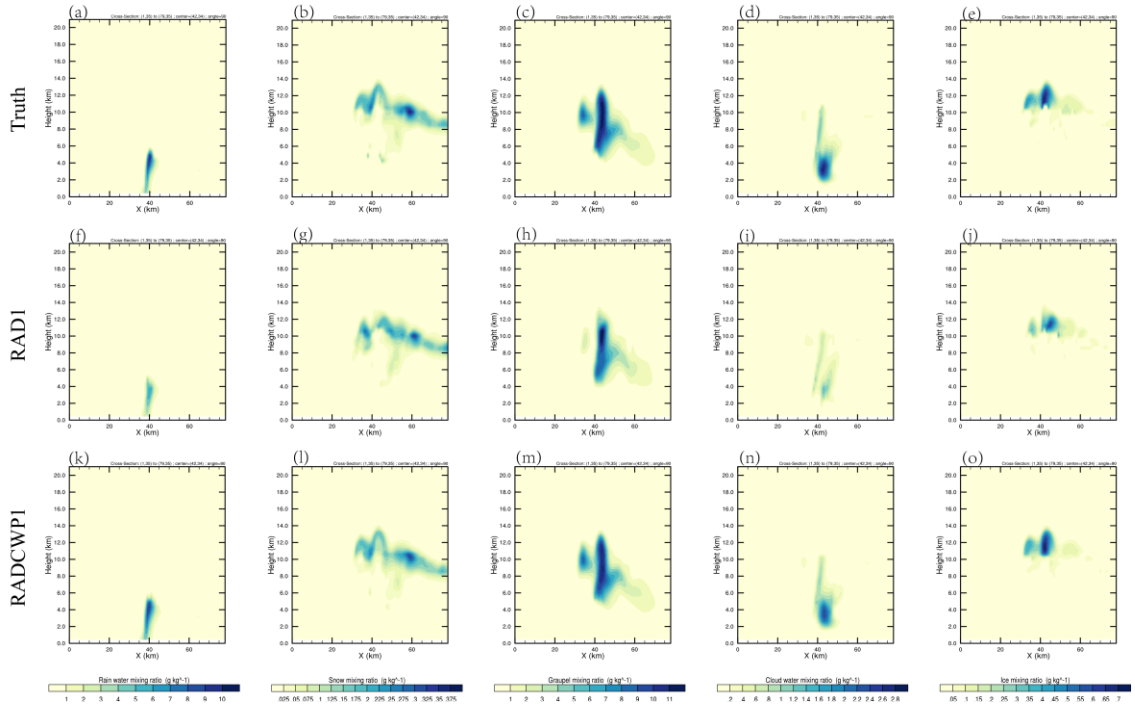

Figure 7. Vertical cross section of five hydrometeor mixing ratios including rain water (a, f, k), snow (b, g, l), graupel (c, h, m), cloud water (d, i, n) and ice (e, j, o) across y = 35km for truth, RAD1 and RADCWP1 at 60 min.

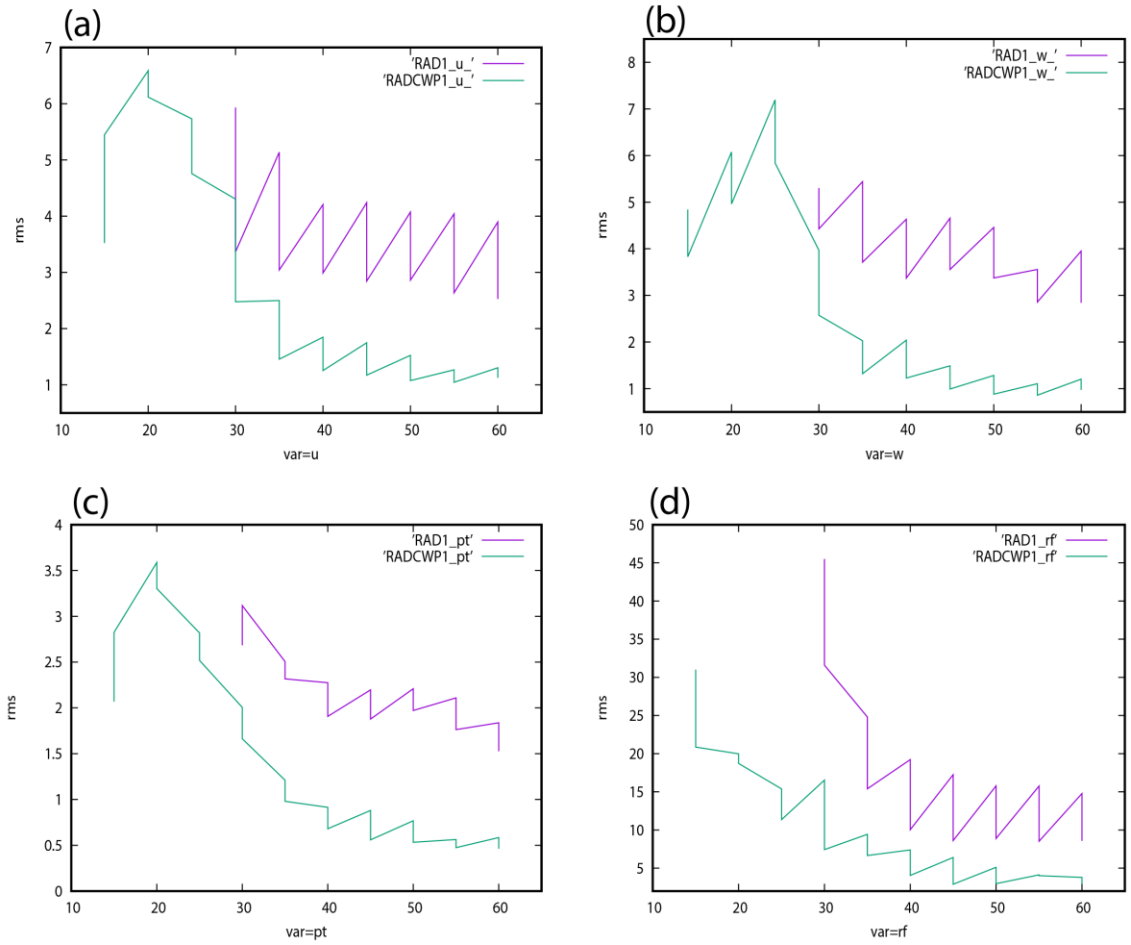

Figure 8. The rms error of the 3DEnVar analysis and forecast for RAD1 (purple) and RADCWP1 (green) experiments. (a) Horizontal wind component u (m s^{-1}); (b) vertical wind component w (m s^{-1}); (c) perturbation potential temperature pt (K); and (d) simulated reflectivity rf (dBZ).

3.3.1 The Verification of Forecasts

To evaluate the impact of assimilating various radar and satellite derived data set for short-term forecasts, a 1-hour free forecast is launched from the first group of experiments. The reflectivity fields at 4 km above the ground for the forecasts are plotted and compared to the truth simulation. In general, all the prognostic variables are appropriately predicted in the forecasts. The RADCWP1 experiment (Fig. 9i-l) produces patterns of reflectivity and vorticity which are nearly the same as that in the truth simulation (Fig. 9a-d). The forecasts for the experiment RAD1 (Fig. 9e-h) generate slightly smaller areas covered by >55 dBZ reflectivity than those in both truth run and RADCWP1. However, assimilating CWP data together with radar data result in a small eastward displacement of the maximum vorticity in forecast as a function of time in comparison with the truth run.

Fig. 10 shows the bias and rms errors for the 1 hour forecast of the control member with and without assimilating CWP data. It shows that the biases for all selected variables are significantly improved (closer to zero) when CWP data are assimilated (Fig. 10 a, c, e, g). The rms errors for the experiment RADCWP1 are smaller than that for the experiment RAD1 for most of the forecast period (Fig. 10 b, d, f, h). But the rms errors become bigger after 50 min of forecast for u component of wind, and after 40 min for vertical velocity and potential temperature for the experiment RADCWP1 when CWP data are also assimilated. At the end of the forecast period, rms errors for nearly all variables are very close to each other, especially for potential temperature and reflectivity.

A set of skill scores including POD, FAR, CSI and HSS between simulated reflectivity fields obtained by the nature run and each experiment over the whole domain is shown in Fig 11. RAD1 and RADCWP1 generate similar FAR, but an interesting phenomenon is that the former has a lower FAR than RADCWP1 experiment at most of time despite excluding clear-sky CWP to prevent spurious convection from triggering. Since RADCWP1 combines CWP data containing non-precipitating cloud properties such as cloud water and cloud ice, and spreads this information in space and to different variables through En3DA, RADCWP1 generates a higher POD than that for the radar DA alone during the forecast period, resulting in a higher CSI and HSS. The discrepancy of CSI and HSS between two experiments decreases with time, and is very similar by 115 min. However, RADCWP1 continually has higher overall skill scores for 50-min forecast from 60 min to 110 min.

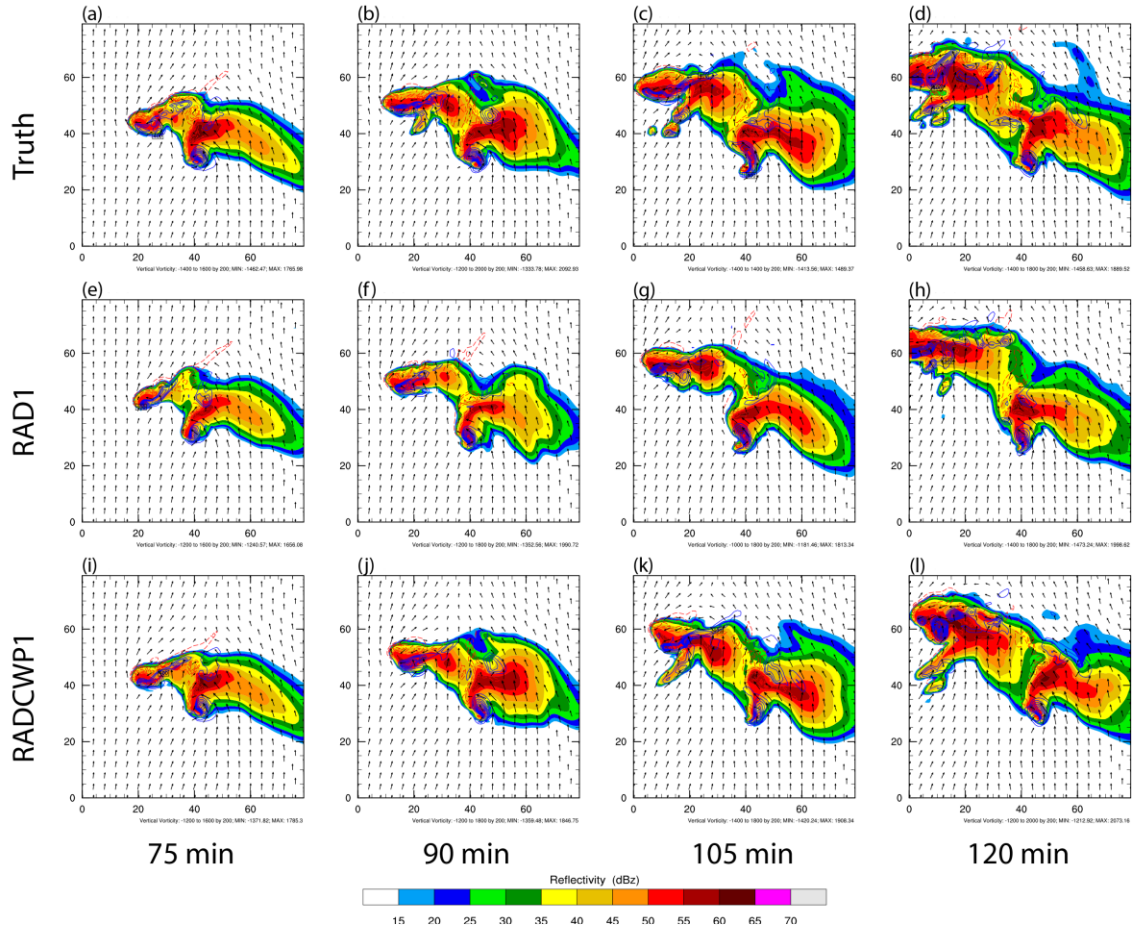

Figure 9. 4-km AGL wind, vorticity and reflectivity from truth (a-d), RAD1 (e-h), RADCWP1 (i-l) at 15-min intervals for 1-hr free forecast initiated at 60 min.

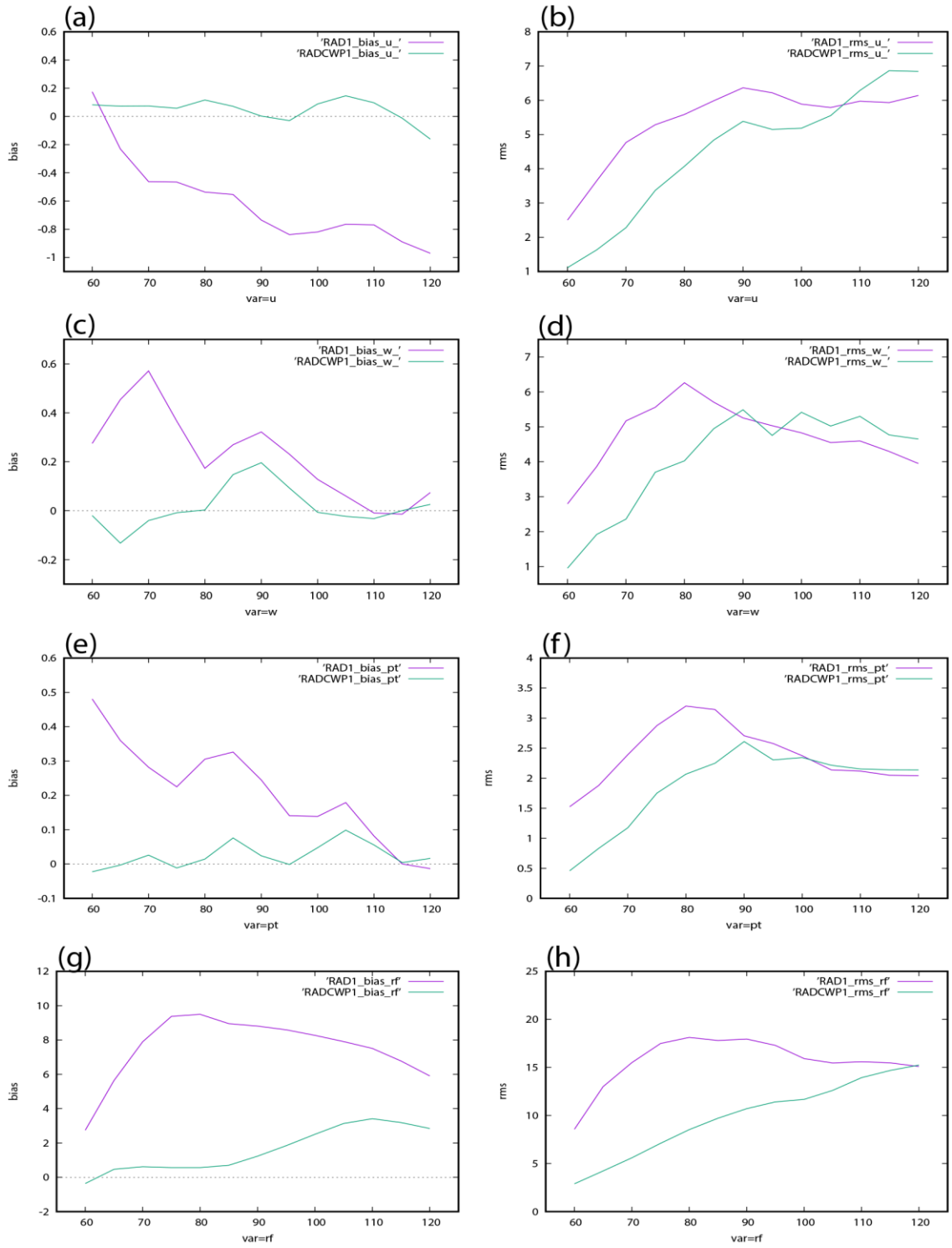

Figure 10. The biases (left panel) and rms errors (right panel) of 1-hr free forecast initiated at 60 min of model time for RAD1 (purple) and RADCWP1 (green). (a), (b) for Horizontal wind component u $(\mathrm{m\ s^{-1}})$; (c), (d) for vertical wind component w $(\mathrm{m\ s^{-1}})$; (e), (f) for perturbation potential temperature pt (K); and (g), (h) for simulated reflectivity rf (dBZ).

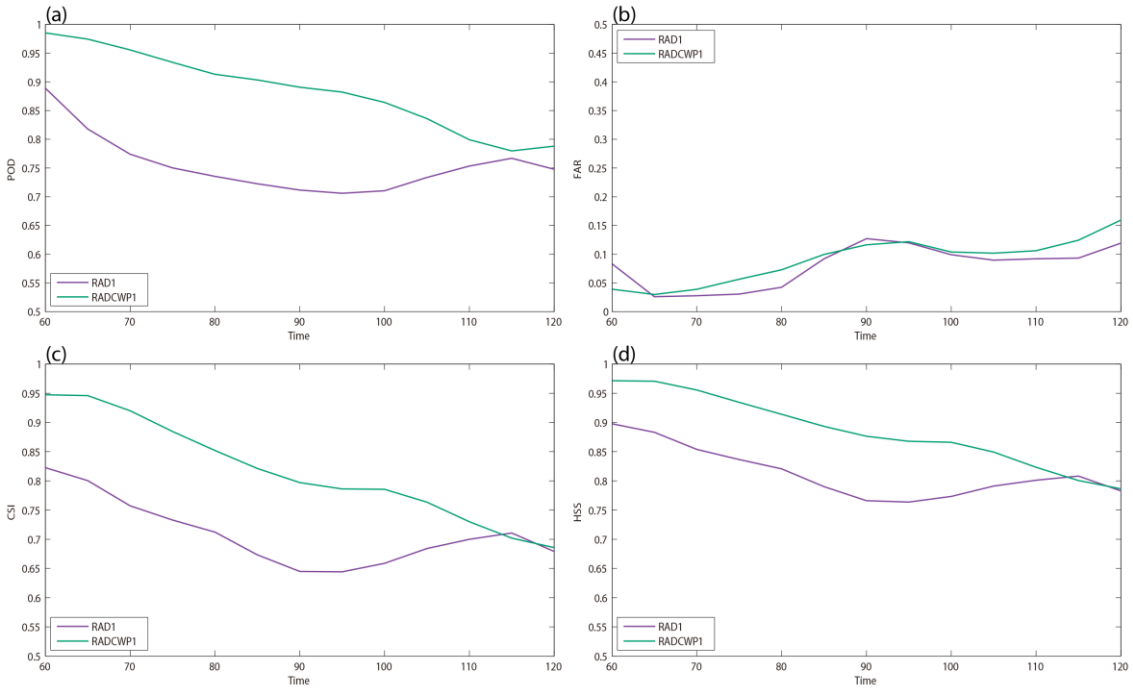

Figure 11. Skill scores including POD (a), FAR (b), CSI (c), and HSS (d) of 1-hr free forecast initiated at 60 min of model time for RAD1 (purple) and RADCWP1 (green).

3.4 The Experiments with Dry Biased Sounding

3.4.1 The Diagnostics of Analyses

The impacts of radar data and satellite retrievals in En3DA analysis are evaluated by another set of experiments using a modified sounding with dry bias. The temperature profile keeps consistent with the original sounding but the dew point temperature is decreased, indicating that the moisture is correspondingly changed. In this way, the CAPE for the new sounding (Fig. 1, red lines) significantly decreases to 1426 J from 3918 J due to the reduced moisture in lower and mid-troposphere. The environment for this case is not good enough to activate convection even if a thermal bubble is given (Not shown). Fig. 12 depicts wind vectors and reflectivity in both horizontal and vertical section at the end of each assimilation cycle. All the vertical cross sections are drawn across y = 35km. From the perspective of wind vectors, the analyses for all experiments look very good because radial velocities are directly assimilated. But if we compare the vorticity or reflectivity patterns, experiments with different observation sources result in totally different biased and inaccurate analyses. RAD2 almost fails in producing two supercells (Fig. 12a). The maximum value of the reflectivity for the left-moving cell is less than 35 dBZ where is greater than 55dBZ in the reference truth (Fig. 5a). Meanwhile the strong vorticity of 1640×10^{-5} s^{-1} associated with high reflectivity > 55dBZ within the right-splitting cell (in truth simulation) is not shown in RAD2. Comparing Figure 12b with Figure 5a, we find that the analysis with only radar data does not well recover the rising motions in both of the upper levels (10-13km AGL) and lower levels (2-4km AGL) and the corresponding narrow area of high reflectivity from the surface to the 14 km above the ground. Slightly weak and discontinuous reflectivity

patterns to the east boundary indicate incorrect analysis of cirrus outflow as well. For the experiment RADCWP2, the analysis looks much better than assimilating only radar data, especially the scope of the reflectivity which is close to true simulation. The supercell (Fig. 12d) indicated by the maximum vorticity and reflectivity basically corresponds well with the truth simulation. However, much stronger reflectivities and chaotic vorticity patterns are displayed in both horizontal section and vertical section. Both left- and right-moving cells look too strong because the maximum vorticity reaches $>1800 \times 10^{-5}$ s^{-1} that is 200×10^{-5} s^{-1} greater than that in the truth simulation (Fig. 5a). When TPW data are assimilated in experiment RADSAT, the precipitating area is approximately identical in shape and coverage compared with the nature truth run (Fig. 12e, f). But a few spurious echoes are generated. The vorticity field is better organized associated with a closer magnitude of maximum vorticity to the true simulation. The analyses for water vapor mixing ratios are very low at the end of the DA cycles for RAD2 and RADCWP2 (Fig. 13c, d, e, f) comparing to the truth simulation (Fig. 13a, b). But more water vapor mixing ratios are added with assimilation of TPW data. This explains that the dry bias in storm environment cannot be corrected by assimilating radar data and satellite CWP data. However, as we mentioned before, the storm environment is fundamentally important for predicting the evolution of the convections. By assimilating TPW data, the dry bias in storm environment is reduced, but it is limited because TPW data contains no information about the vertical distributions of water vapor.

A quick review of temperature field in mid-level and near surface is given in Fig. 14. In general, assimilating only radar data generates the worst analysis among RAD2,

RADCWP2 and RADSAT experiments. The representations of cold pools (Fig. 14a) and warm cores (Fig. 14b) embedded in the storm are hard to see for the first experiments. The temperature structure is improved in RADCWP2 (Fig. 14c, d) since cold pool can be found associated with the storms, but it is too cold and some splitting cold areas are not expected. Comparing Figure 14e and 14f with the others, we can find that the analysis with TPW data is the best one among three experiments due to the improved magnitude and location of cold pool and warm core appear.

Figure 15 shows the rms errors of 4 selected variables (horizontal wind u, vertical wind w, potential temperature pt and reflectivity rf) for this second group of experiments. Results indicate that the rms errors for RAD2 are generally greater than the other two experiments over all selected variables except for reflectivity during the early DA cycles. Assimilating CWP data does not alter rms errors to a significant degree. However, assimilating TPW does reduce u and w rms errors compared to the other experiments highlighting the importance of adequately sampling the near storm environment. The errors of wind and temperature fields in RADCWP2 rise and exceed those in RAD2 experiment initially, then decrease after radar data is assimilated and finally become smaller than RAD2. Overall, the accuracy of the analysis improves when TPW data are assimilated. Further impacts of assimilating TPW are shown in the forecast evaluation section.

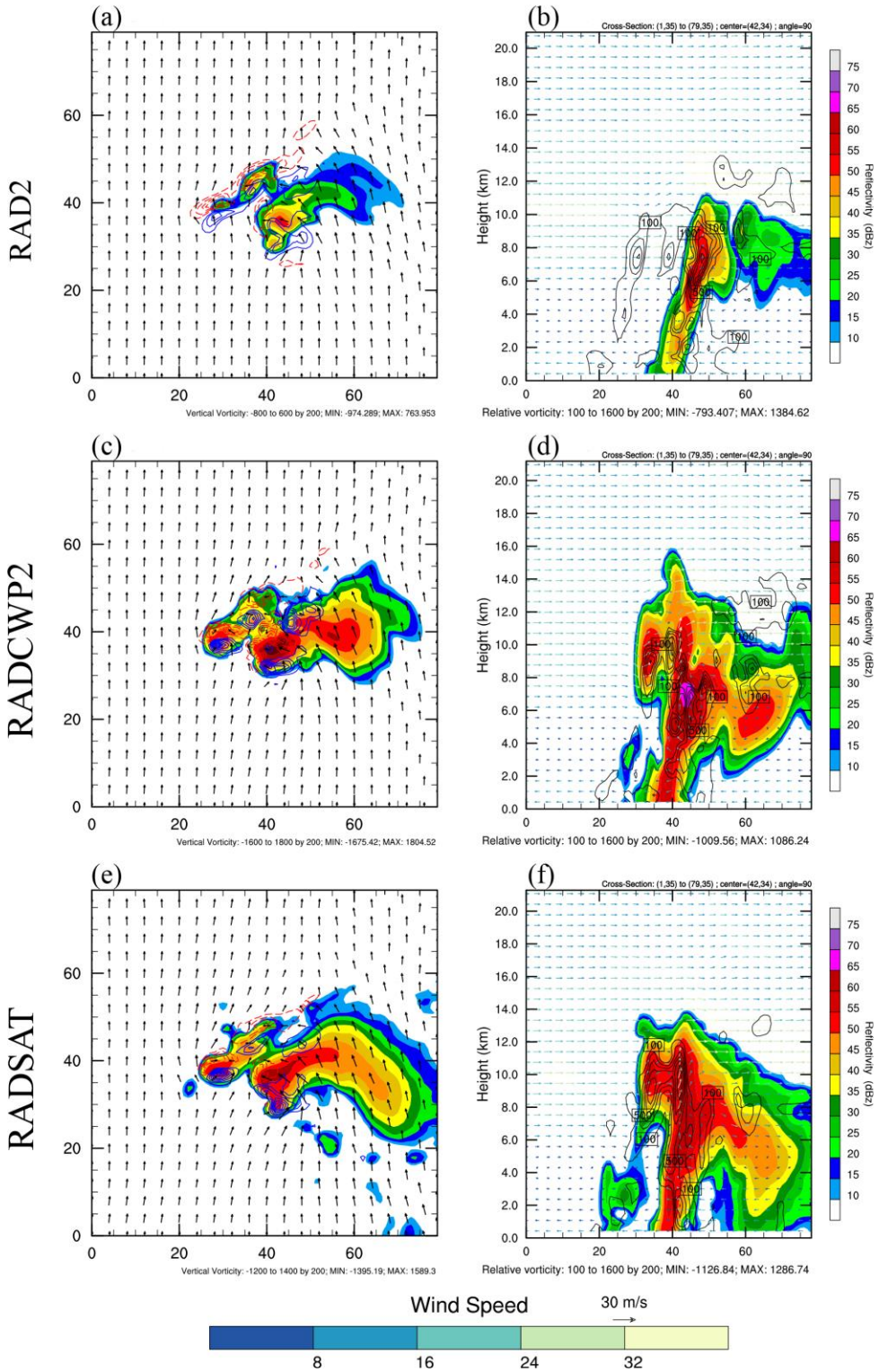

Figure 12. As in Fig 5, but for experiment RAD2, RACWP2 and RADSAT.

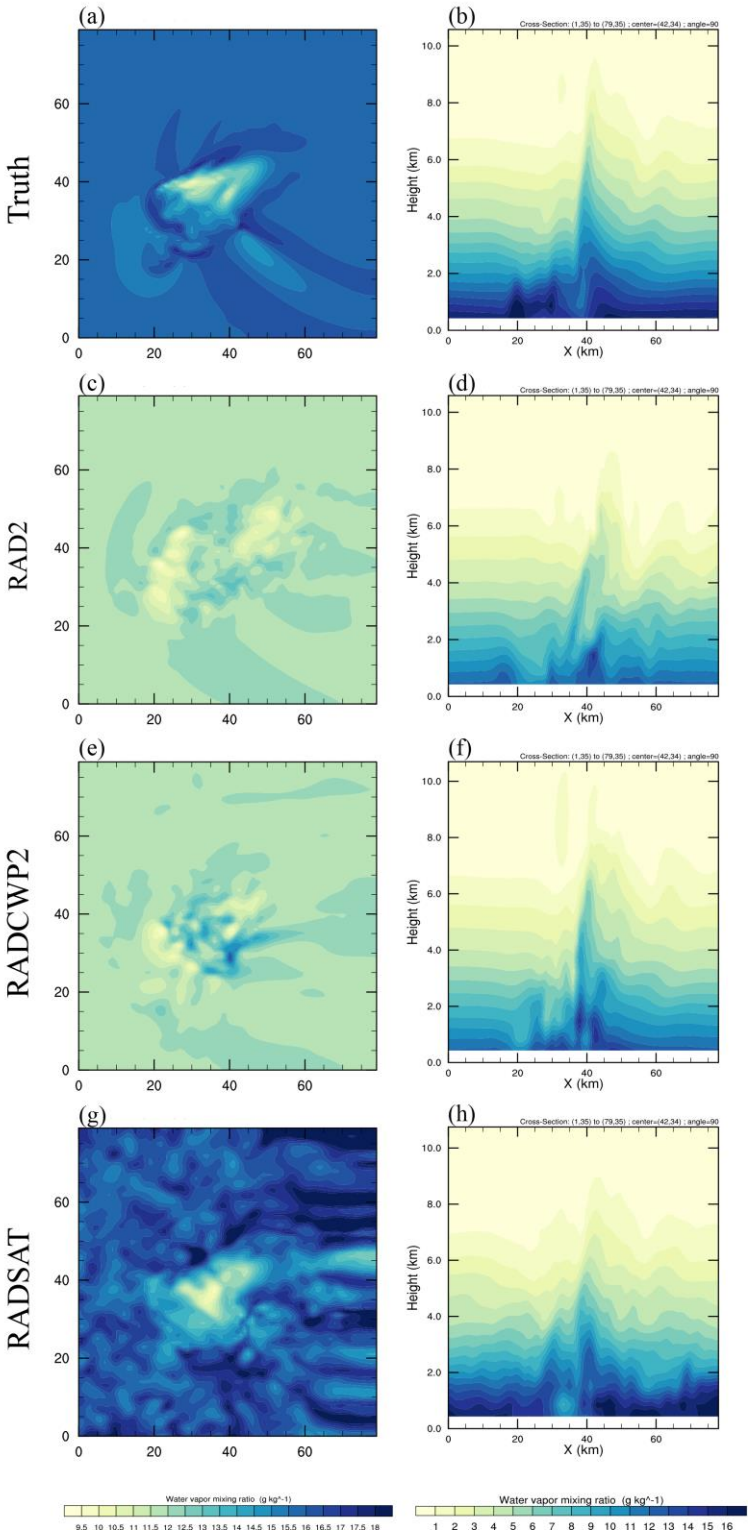

Figure 13. Water vapor mixing ratio in horizontal cross section at 4km AGL (a, c, e, g) and vertical cross section at y = 35km (b, d, f, h) for truth, RAD2, RADCWP2 and RADSAT at 60 min.

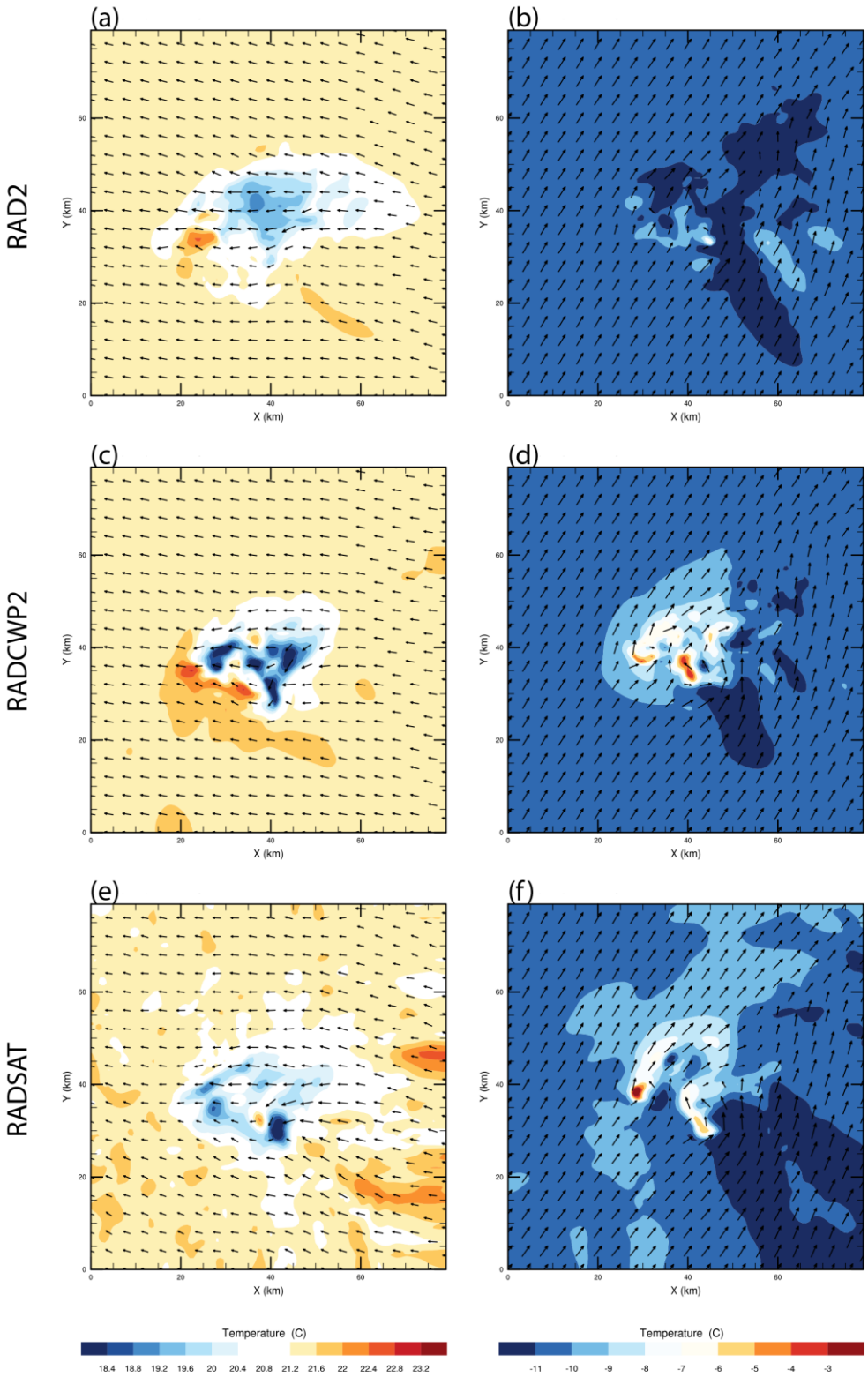

Figure 14. As in Fig. 6, but for experiment RAD2, RADCWP2 and RADSAT.

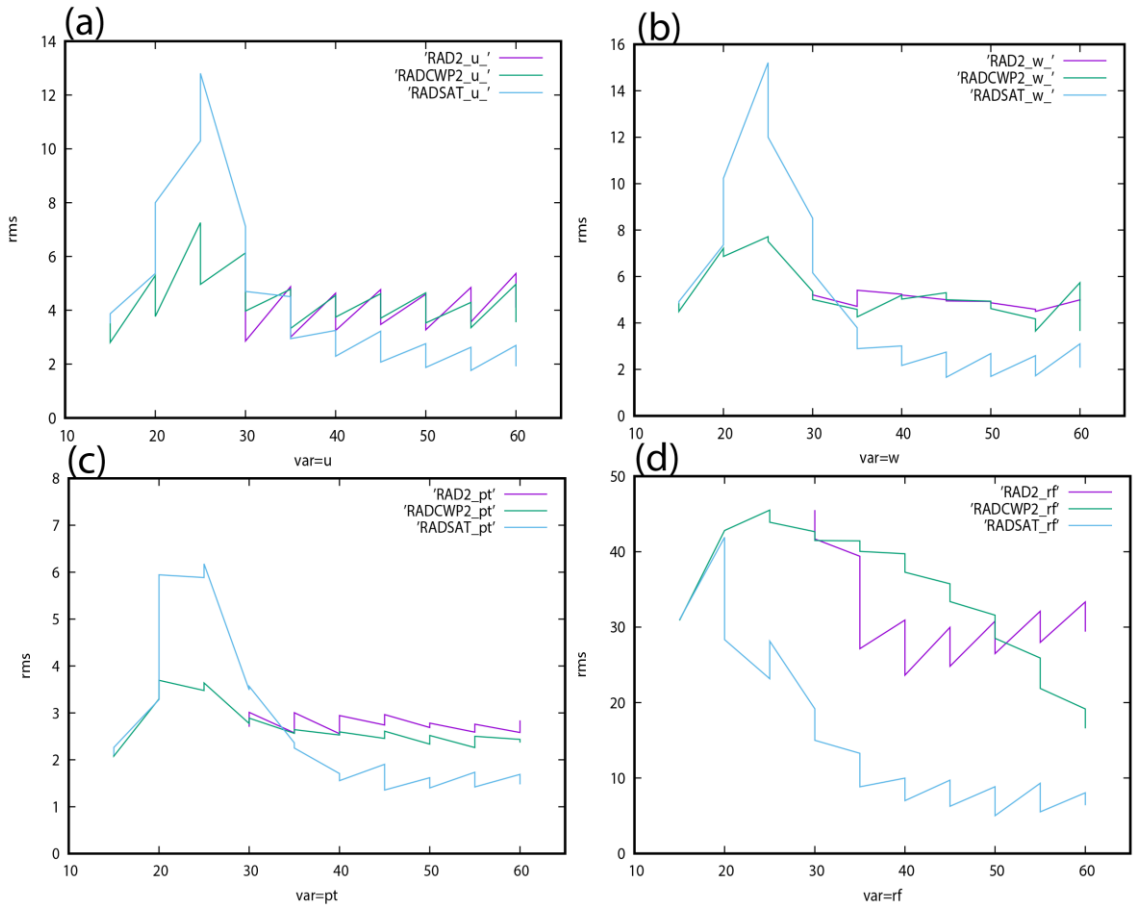

Figure 15. As in Fig. 8, but for experiment RAD2 (purple), RADCWP2 (green) and RADSAT (blue).

3.4.2 The Verification of Forecasts

Similar to the previous session, the impact of various data in short time forecast under the imperfect storm environment with dry bias is discussed here. Obviously the very weak initialized storm cell after 30-min DA cycles quickly dies in 20 min after the forecast is launched for the experiment RAD2 when only radar data are assimilated (Fig. 16a-d). Though the major right-moving storm is much better initialized in RADCWP2 when CWP are also assimilated, it also dies after 30 min forecast (Fig. 16e-h). The reason of quick dissipation of the storm is simple, i.e., the storm environment is not correctly generated by DA even when both radar data and CWP data are assimilated. When TPW data are assimilated in the RADSAT experiment, the storm environment gets corrected in some degree so that the two storm cells are produced in right time and right place even with small spurious cells around. The left-splitting storm which is not produced in previous experiments is partly captured by RADSAT because more adequate low-level moisture and more accurate instability of environment are produced by the DA. Though the intensity and expand area of these two storm cells generally maintains well during the 60-min forecast period (Fig 16. i-l), small spurious cells do grow and develop around the major storms by the end of 1 hour forecast period. The similar situation also appears in many real data case studies (Fierro et al. 2016; Stensrud and Gao 2010).

Other statistics are plotted for three experiments and shown in Figure 17. These clearly demonstrate that the biases and rms errors for reflectivity can be significantly reduced when TPW data assimilated (Fig. 17e, f). The results of both bias and rms errors look mixed for other three selected model variables (17a-d). Finally, the same set

of skill scores that compared the second set of experiments with the truth simulation are also plotted in Figure 18. Basically, the RAD2 essentially has no skill for all forecast times. RADCWP2 shows some skill in a 30-min forecast but almost no skill thereafter. RADSAT generates higher skill scores than both RAD2 and RADCWP2. This result clearly indicates that incorporating TPW data for correcting storm environment is very helpful. But only using vertical integrated moisture data is not good enough to precisely adjust vertical moisture structure of storm environment.

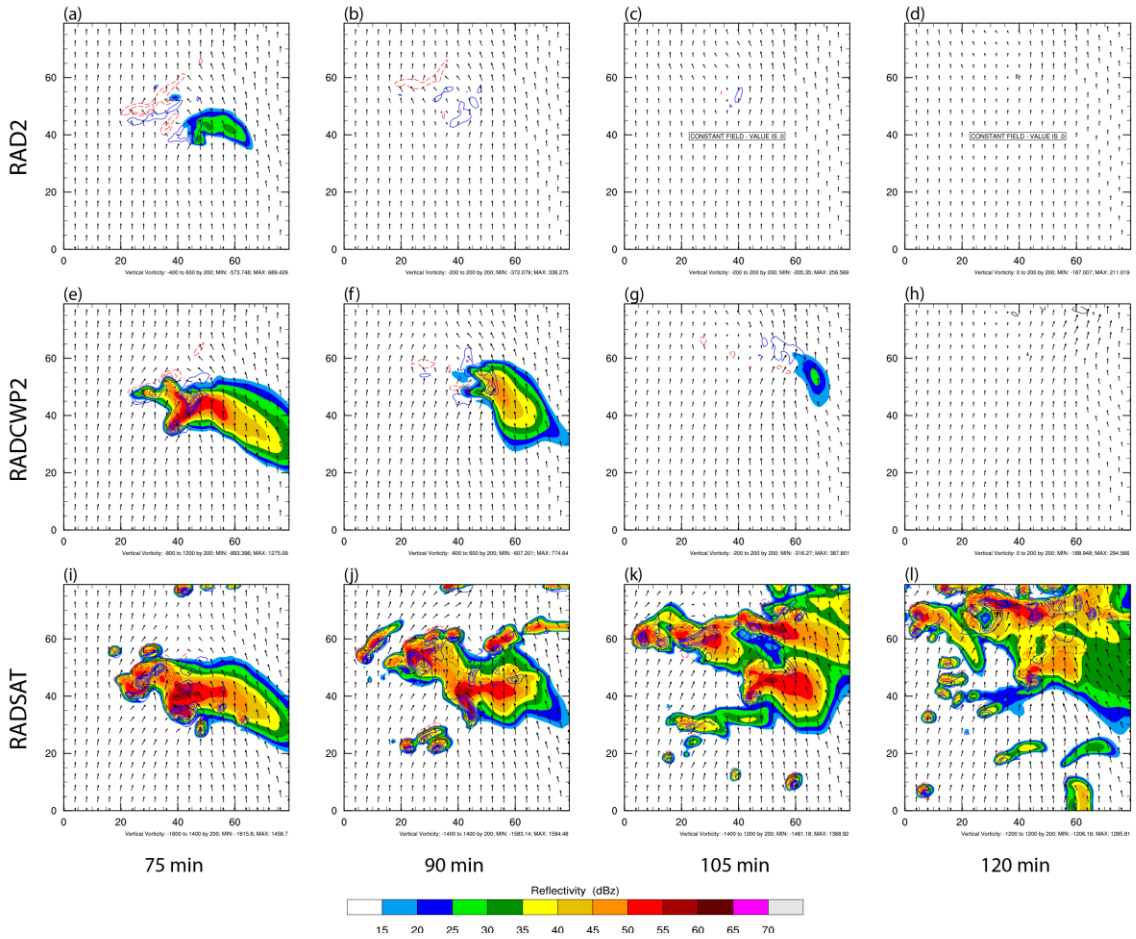

Figure 16. As in Fig. 9, but for experiment RAD2, RADCWP2 and RADSAT.

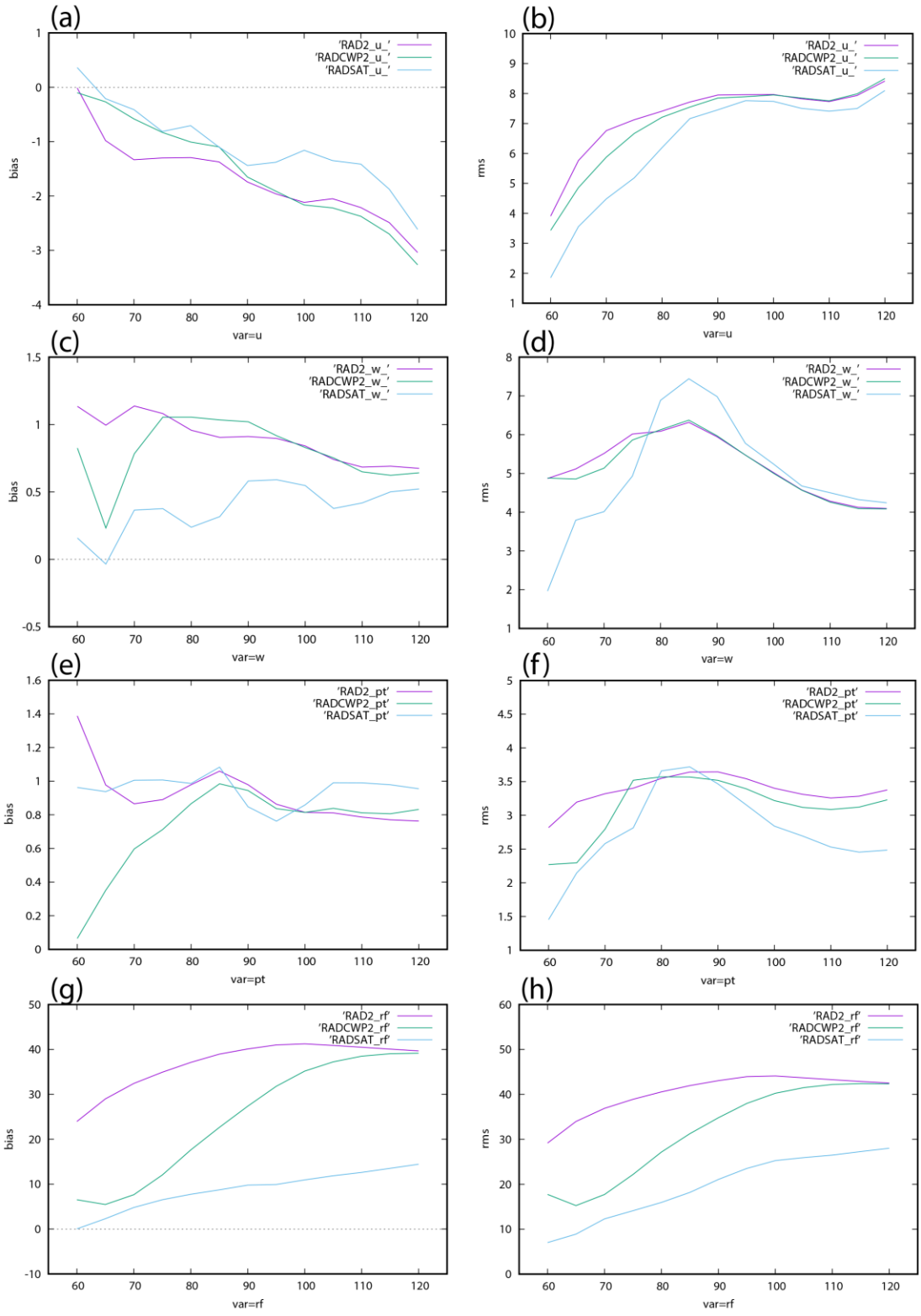

Figure 17. As in Fig. 10, but for experiment RAD2 (purple), RADCWP2 (green) and RADSAT (blue).

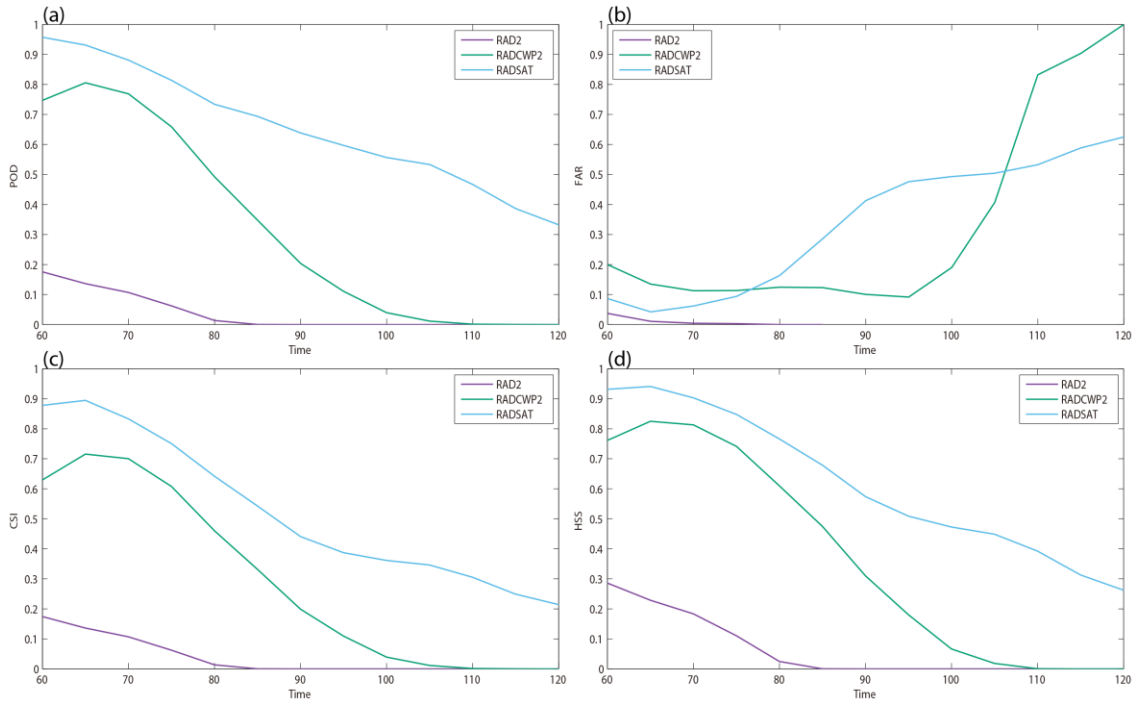

Figure 18. As in Fig. 11, but for experiment RAD2 (purple), RADCWP2 (green) and RADSAT (blue).

3.5 Summary and Discussion

The experiments with correct environment utilize the radar and CWP data in storm-scale DA. The qualitative and quantitative analyses, including horizontal and vertical storm structure, lower difference of hydrometeor variables between experiments and truth as well as steeper decreasing of rms errors, demonstrate faster spin-up time for early assimilating satellite data. The magnitude and coverage of either dynamic, thermodynamic or hydrometeor fields are approximately recovered in two experiments for both analyses and forecasts. It is worth taking note of big improvements in experiment assimilating both radar and satellite data. However, like almost of previous OSSEs for convective scale DA, all the above experiments are done under a perfect storm environment, which does not always reflect real-world conditions.

Unlike the experiment with original sounding, the results of experiment with dry biased environment are totally different. Assimilating only radar data totally fails to recover the supercell in both DA cycles and 1 hour free forecast. By including CWP data, the storm structure is improved in analysis but the RMSEs of selected variables are still poor as RAD2 experiment. The free forecast from the initial state with assimilating CWP data shows that the supercells assimilated into WRF model quickly dissipates in 30 minutes. It implies the dynamic and thermodynamic fields are unbalanced and the environment prevents the convection from maintaining. When the TPW data are assimilated, the analyses are largely enhanced with much lower RMSE. The forecast results show that the storm structure keeps developing in the next 1 hour accompanied with higher skill scores as well.

The results of this study may provide guidance for satellite retrieval data in storm-scale data assimilation as well as convection-allowing NWP.

Chapter 4 The 25-26 May 2016 Solomon Tornadic Supercell - A Real Data Case Study

4.1 The Case

On 25 May 2016, atmospheric conditions in north central Kansas were very favorable for the development of severe thunderstorms. An isolated supercell thunderstorm formed over Ottawa County in the late afternoon on that day. Then the storm continued to develop and to generate 4 tornadoes during the evening. The first tornado was reported at approximate 2308UTC 3 miles south of Minneapolis but only lasted around 1 minute. The same thunderstorm kept moving to the southeast and then the second tornado was a long-track violent EF-4 tornado that sustained about one and a half hours since 0007UTC on 26 May 2016 with 0.5 mile maximum width (Fig. 19). The supercell thunderstorm moved into Morris and Wabaunsee counties and produced 2 more tornadoes before its dissipation. Here our study focuses on the major thunderstorm since 0000UTC.

The long track tornadic thunderstorms on 25-26 May 2016 were observed by five WSR-88D radars including KUEX, KICT, KOAX, KTWX and KEAX. As shown in Fig. 20, The KTWX radar observed the low to middle layers of this storm because it is the nearest one to the storm in comparison with other radars. At the meantime, the other four radars provided information of the upper portions of the storm. Combining information from these radars can depict the whole structure of this thunderstorm but still may miss details between radar beams. The GOES-13 satellite documented this severe weather event as well. GOES-13 retrieved cloud water path data are used in this

case study while the total precipitable water data is discarded because it is not available from GOES-16 in the early 2016.

However, a big challenge still exists in this case. The traditional observations, such as rawinsondes are far away from the storm. The mesoscale environment that supported the storm did not well captured. At 0000UTC on 26 May 2016, a rawinsonde launched from Topeka, KS (TOP), around 90 miles east to the storm, only captured weak veering wind shear with 6 m s^{-1} southerly winds at surface and ~15 m s^{-1} westerly winds at 500 hPa. The TOP sounding showed that atmosphere had 1427 J kg-1 CAPE and 179 J kg-1 convective inhibition (CIN), indicating a weakly unstable environment. Another rawinsonde launched from Dodge City, KS (DDC), approximate 165 miles southwest to the storm, provided a similar weak atmospheric instability but with 28 m s^{-1} vertical wind shear, 1905 J kg-1 CAPE and 164 J kg-1 CIN respectively. Therefore, this is a good case to study the impact of satellite retrieval data in convective DA and NWP.

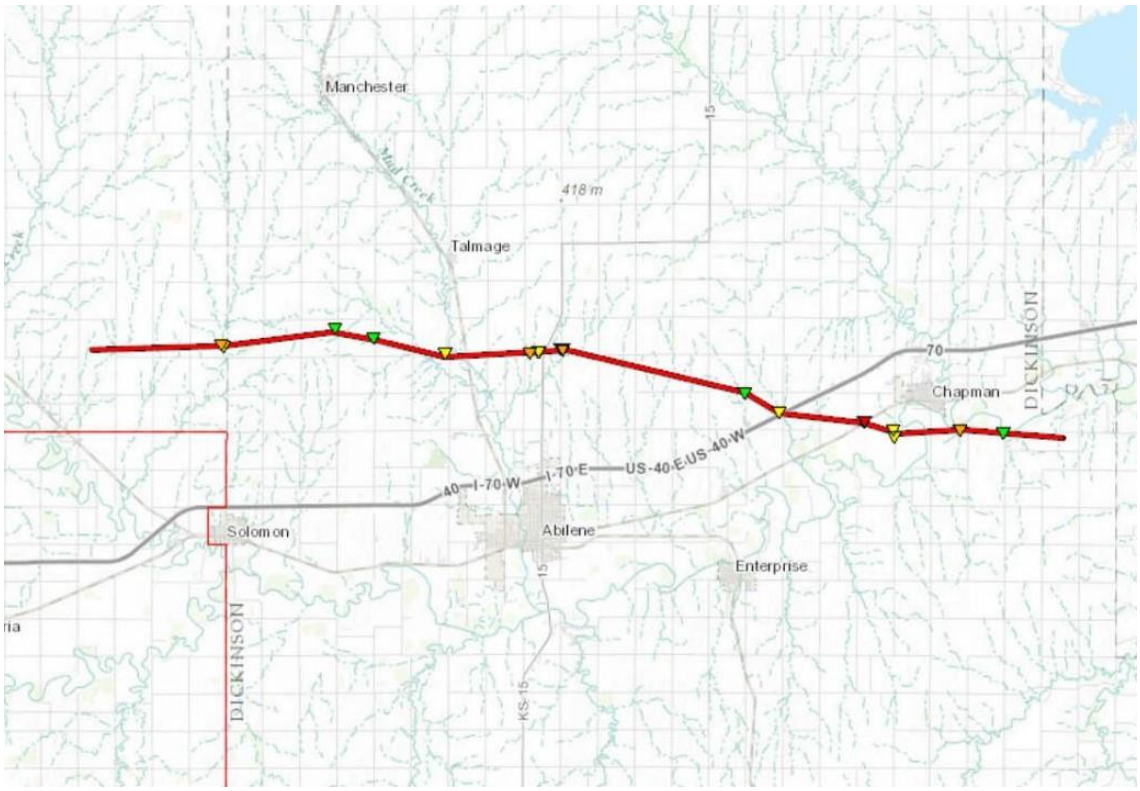

Figure 19. NWS track of tornadoes/thunderstorms occurred on 25-26 May 2016. Triangles along the track show the positions and intensities of tornadoes: blue (EF-0); green (EF-1); yellow (EF-2); orange (EF-3); red (EF-4); purple (EF5).

4.2 Experimental Design

Both the WRF-ARW model and En3DA system described in Chapter 1 are employed in this real data case. The control member is initialized from North America Mesoscale Forecast System (NAM) at 2100UTC on 25 May 2016. Additional 25 ensemble members are then generated by adding random noises to the control member. Random noises are drawn from model errors which are estimated by hourly-updating High-Resolution Rapid Refresh-Ensemble (HRRRE). Three-hour (2.5 hours for satellite experiments, Fig. 21) ensemble forecasts for the control and 25 ensemble members are launched once they are initialized. An experiment without DA as well as three DA experiment are performed to investigate the impact of assimilating radar data and CWP data through En3DA system (Table 3). The first experiment without any data assimilation is called "NoDA". In the second experiment (CWP) only assimilates CWP data. The third one (RAD) only assimilates radar data and the final experiment (RADCWP) assimilates both radar and CWP data. The RAD experiment starts from 0000UTC and end by 0100UTC on 26 May 2016. Other experiments that use satellite data start on 2330UTC on 25 May 2016 that is 30 minutes prior to the RAD experiment, similar to OSSEs.

TABLE 3. Assimilation experiments of case study on 26 May 2016.

Experiment	Vr + Reflectivity	CWP
NoDA	×	×
CWP	×	√
RAD	√	×
RADCWP	√	√

All experiments are conducted in one-way nested domains. The coarser domain has 241 and 161 grid points with 4-km horizontal grid spacing in west-east and south-north direction separately. The finer domain has 161 and 121 grid points with 2-km resolution in west-east and south-north direction separately. Both domains have 51 vertical layers with dense layers near the surface but constant vertical spacing of 460 m from 2 km to 20 km AGL (model top, 50hPa). All observations are assimilated into the inner (finer) domain. The model domain is shown in Fig. 20. The single-moment 5-category Thompson scheme as well as 1.5-order TKE closure are used as parameterizations for the model run. Longwave and shortwave radiation schemes are adopted for this real data case. Additional model details are given in Table 4.

TABLE 4. WRF-ARW 3.8 model configurations.

Domain	Outer	Inner
Time step	12	6
Horizontal Advection	5^{th} order	
Vertical Advection	3^{rd} order	
Turbulence Parameterization	1.5-order TKE closer	
Microphysics Scheme	Thompson	
Cumulus Parameterization	Off	
Longwave Radiation Scheme	RRTMG	
Shortwave Radiation Scheme	RRTMG	
Radiation Scheme Interval	15 min	5 min
Land Surface	Noah Land Surface	
Surface Layer Scheme	Eta Similarity	
PBL Scheme	MYJ Scheme	
Urban Surface Scheme	Off	

As we all known, any errors in radar observations may cause serious biases in the analysis after DA. Therefore, before assimilating radar data into NWP model, quality

control is required to prevent the DA system from using wrong observations. This procedure includes “bad” observations rejection, Doppler-velocity dealiasing etc. After the process of quality control, the radar data are projected from the observation space onto the model space by quadratic spatial interpolation (Brewster 2005). This can be considered as “data thinning” process because data from NEXRAD network has a spatial resolution of ~250 m that is much smaller than model spacing (2 km) in this case.

CWP is a kind of satellite product retrieved from GOES-13. It has been quality controlled after complicated algorithm of derivation. The quality of observations is provided with data set as well. Observations are separated into liquid phase and ice phase with confidence or suspicion. On the other hand, the resolution of geostationary satellite typically has a resolution from 2 km to a few kilometers near 39°N. It is larger than the model spacing in this case. Therefore, the “data thinning” process is not necessary here. The satellite retrieval CWP data are directly used in En3DA system without any preprocess.

Fig. 21 plots the flow chart for this real data case. An isolated set of experiment that only use the CWP is also set up and starts from 2330 UTC. For this particular case, CWP data from GOES-13 is available at 15-min interval in operation but the data at two time levels 0000UTC and 0030UTC are missing. In addition, surface observations from NCEP Meteorological Assimilation Data Ingest System (MADIS) are also applied at 0000UTC and 0100UTC for each DA experiment. By the end of the DA cycles, a 1 hour free forecast of control member is launched from 0100UTC. The exactly same configuration for DA and WRF model described in this section are applied to all

experiments during the DA and forecasts cycles. Also, the mass continuity equation is used as a weak constraint. Zero reflectivities and clear-sky CWP are assimilated to suppress spurious cells for all real data experiments.

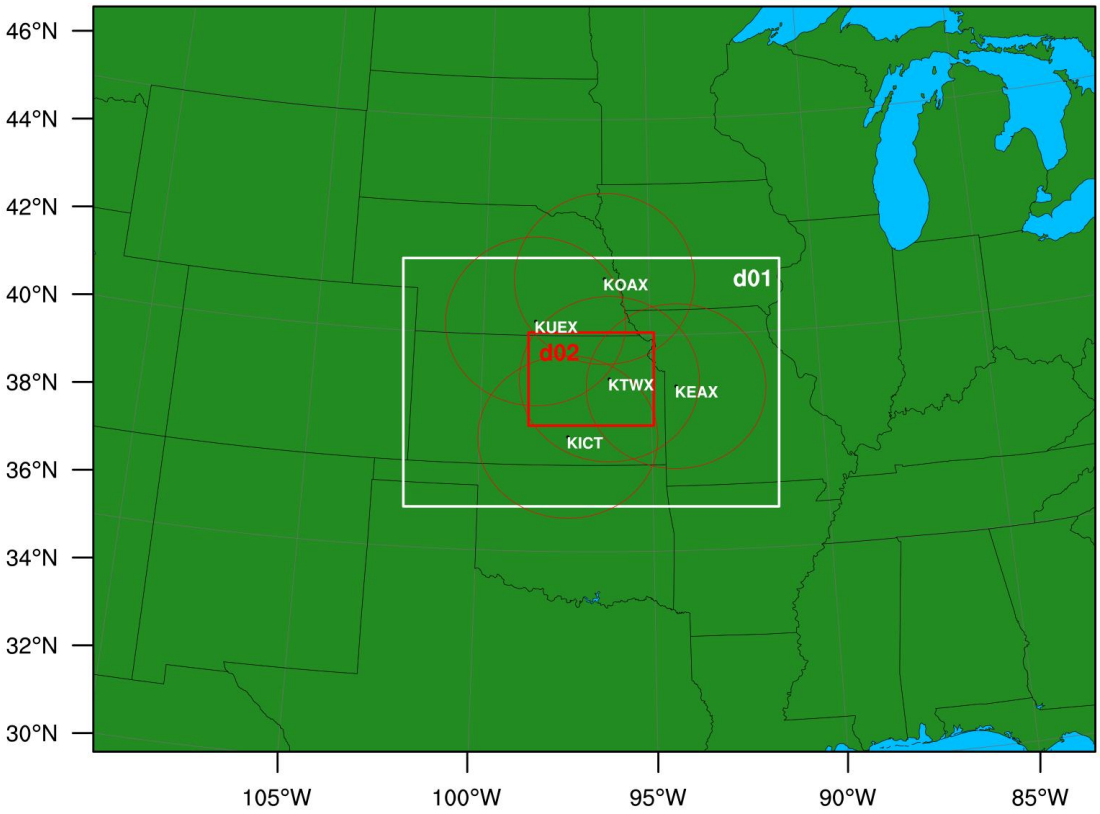

Figure 20. Map showing the 4-km resolution outer experimental domain labeled "d01", 2-km resolution inner domain labeled "d02", and coverage of the 5 WSR-88Ds (KOAX, KUEX, KTWX, KEAX, KICT) assimilated into the inner domain "d02".

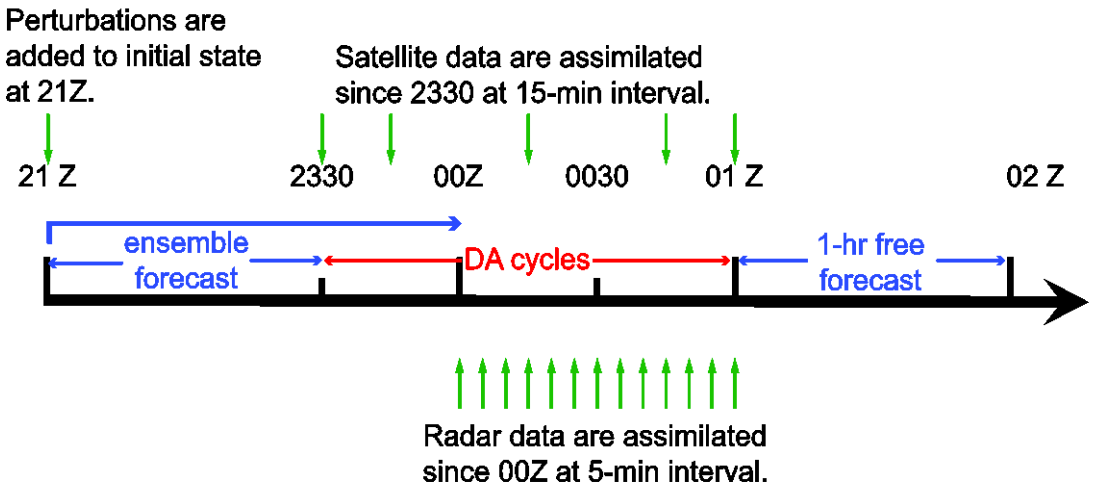

Figure 21. As in Fig. 4, but for the experiments listed in Tab. 3.

4.3 Analysis Results

Fig. 22 exhibits the composite reflectivities for each experiment at two different times 0030UTC and 0100UTC. The NoDA experiment shows that a cluster of spurious storm cells appears along the southern boundary of the inner domain which is not supported by the observations through the DA period (Fig.22 c-d). With the assimilation of cloud water path data in the CWP experiment, reflectivities are widely spread in the center of the inner domain (Northeast Kansas). The precipitating area in CWP experiment covered by > 35dBZ is much larger than that indicated by the observations especially at 0100UTC (Fig.22 f vs b). However, assimilation of only radar observations produces a totally different result. After 30 minutes of radar data assimilation, the supercell storm appears in the right location. The pattern and coverage of reflectivity are closer to the observations at both times (Fig.22 g, h vs a, b), but the storm is relatively weaker than the radar observations. When radar and CWP data are assimilated simultaneously, the analyses look much better. By the end of the DA cycles (0100UTC), the two major storms as well as the small north-splitting cell are fairly recovered (Fig.22 j vs b). Obvious spurious storm cells near the southern domain boundary are almost suppressed in all DA experiments.

The vertical sections of hydrometeors at 0100UTC for three DA experiments are depicted in Fig.23. Since the maximum vertical velocity for experiments with assimilated radial velocity (Fig.23 j) is located at x = 116km and y = 96km, the west-east vertical sections are plotted across the model grids y = 96km. It is not surprising that cloud water and cloud ice cover more areas associated with high content in CWP experiment (Fig23 a, b vs f, g). This is due to the fact that CWP data contain direct

information about cloud water and cloud ice. It is worth noting that the hydrometeors related to the reflectivity are largely enhanced as well in RADCWP experiment (Fig.23 k-o). Especially, the maximum value of rain water is significantly increased from 1.6 g kg^{-1} in RAD to over 8.7 g kg^{-1} in RADCWP. On the other hand, the maximum of graupel maxing ratio hits 11 g kg^{-1} in RADCWP compared with 1.7 g kg^{-1} if only radar data are assimilated. The improvement of snow analysis is also observed but not as noticeable as the rain and graupel.

The temperature at 2 m, wind field at 10 m and relative vorticity at 3 km AGL for all four experiments at same two different time 0030UTC and 0100UTC are shown in Fig. 24. After several DA cycles, the patterns of cold pool are distinguishable between experiments. The cold pool is too spread in CWP experiment. By the end of DA cycles, it covers almost 10 counties with nearly homogenous distribution in CWP experiment. In RAD experiment, the coverage of cold pool is shrunk but more small structures appear near the storm. The cold pools associated with the storms in Ottawa and Dickinson particularly strengthens and is continually strengthening with the cycle moving forward (Fig. 24 e-f). In the CWP experiment, the vorticity field looks more disarranged and many split cells fall in Ottawa and Dickinson County. But for two other radar data related experiments, the whole dynamic field looks more organized. Upon closer inspection of Fig.24 (g) and (h), it can be concluded that assimilating both radar and CWP data provides the best results with cohesive low level storm structure. The area of cold pool as well as stronger vorticities within the storm are more reasonable analyzed in RADCWP experiment. But this estimation should be further proved with the forecast verification.

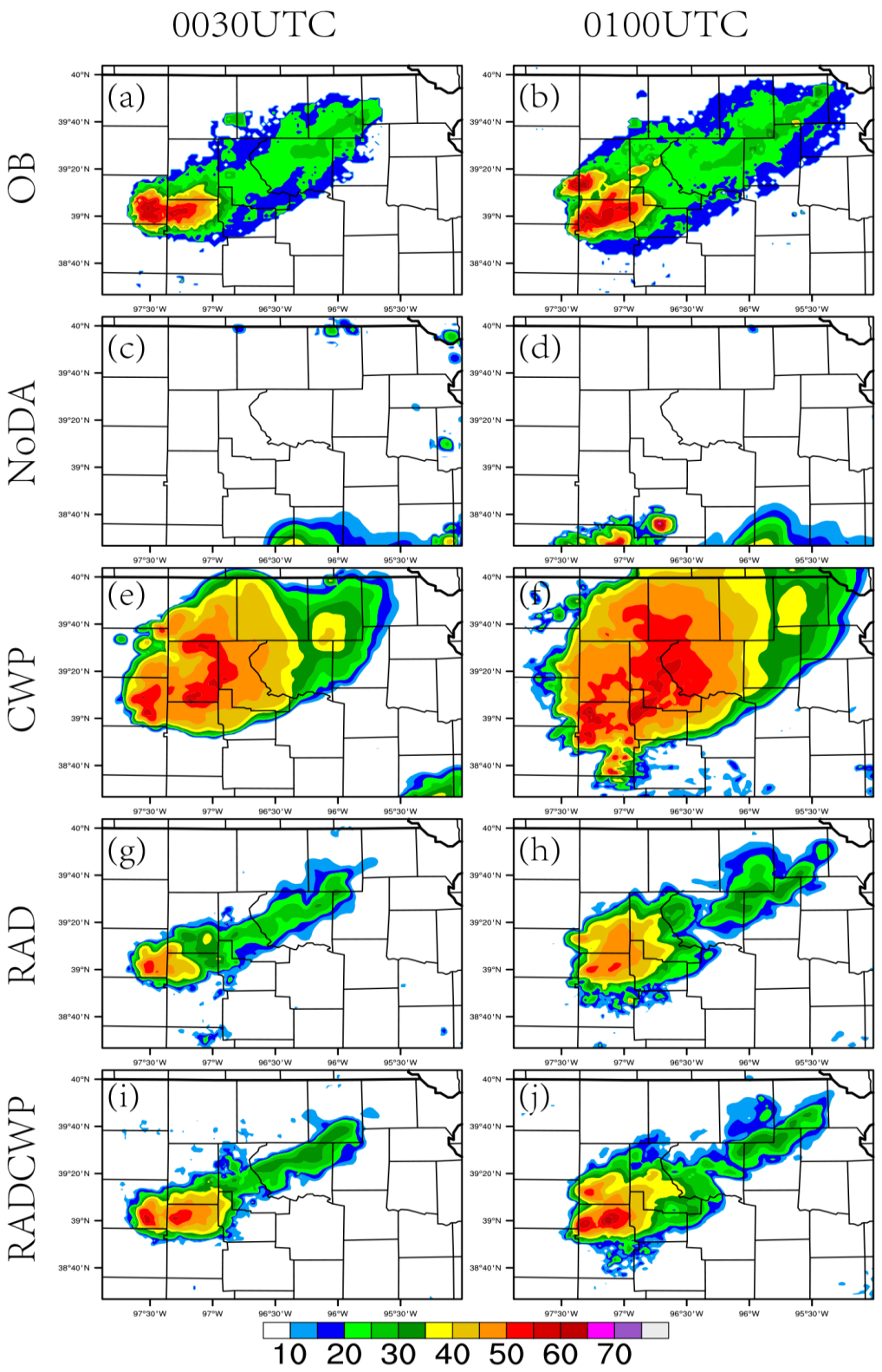

Figure 22. Composite reflectivity for (a-b) observation, (c-d) NoDA experiment, (e-f) CWP experiment, (g-h) RAD experiment and (i-h) RADCWP experiment at 0030UTC and 0100UTC.

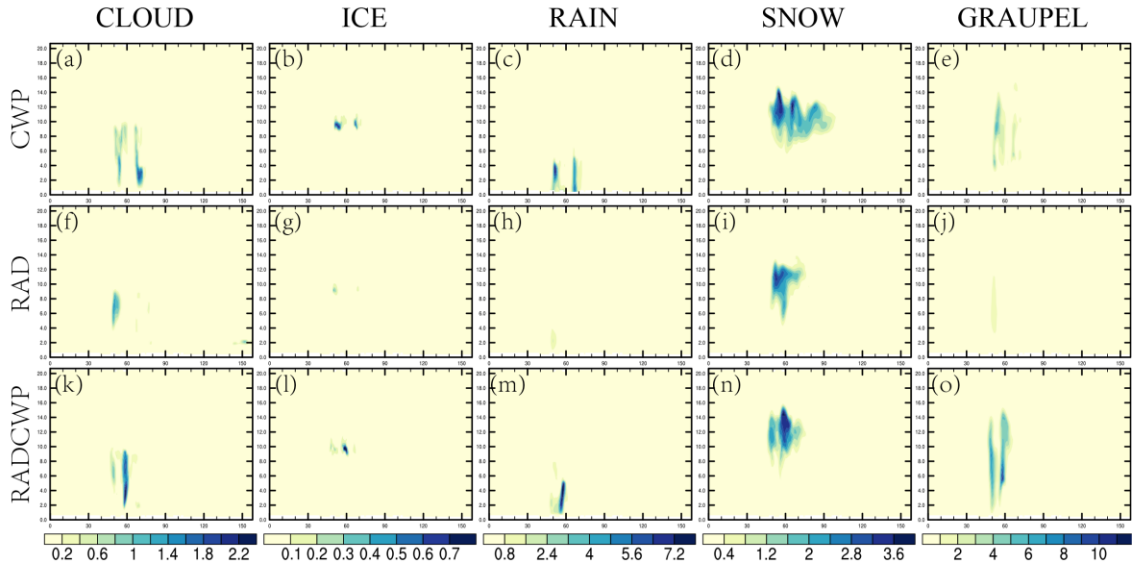

Figure 23. Vertical cross section of five hydrometeor mixing ratios including rain water, snow, graupel, cloud water and ice across y = 96km for CWP, RAD and RADCWP experiments by the end of cycling 0100UTC.

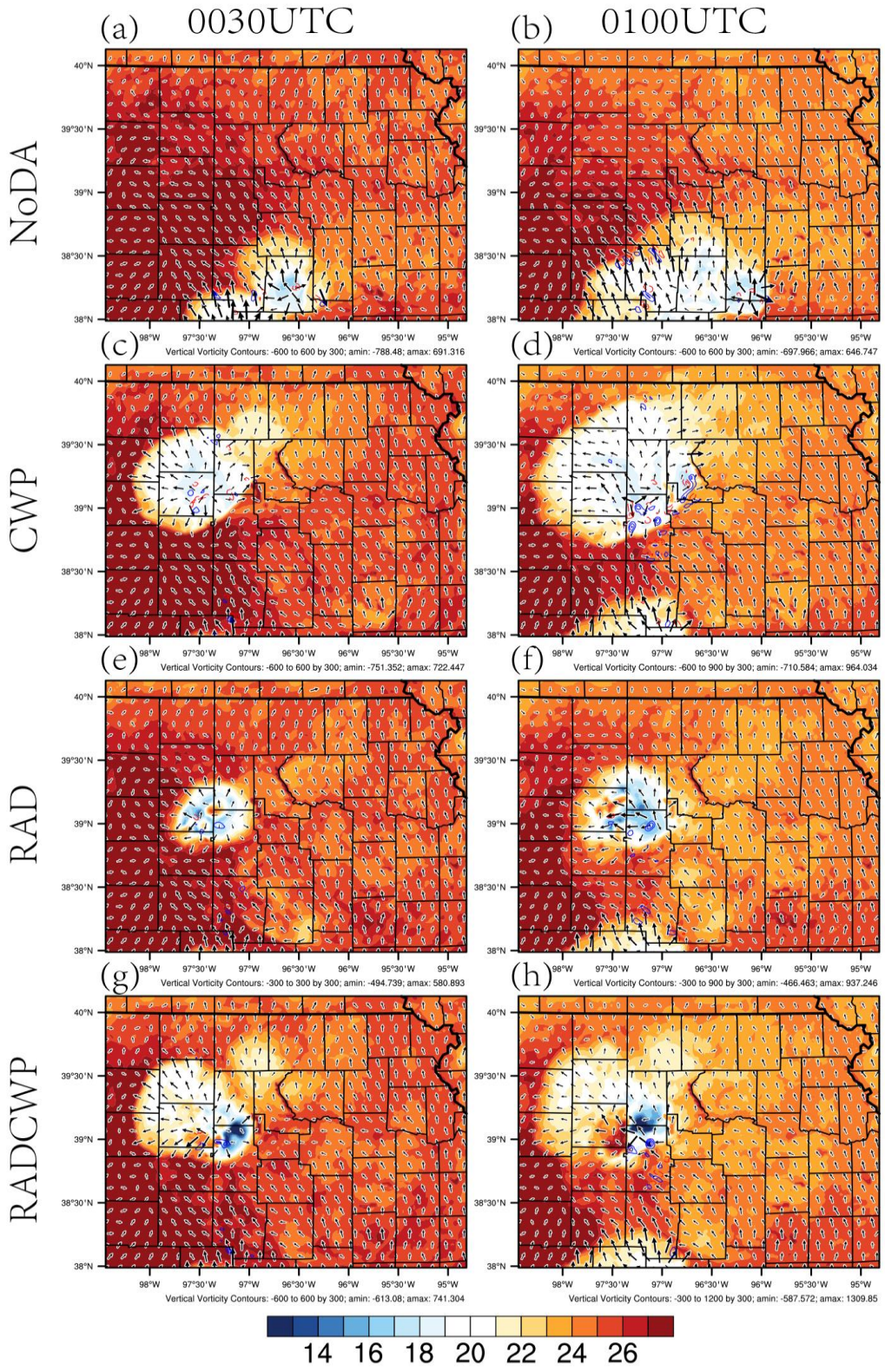

Figure 24. Surface temperature (2-m temperature), wind vector (10-m wind) and relative vorticity at 3km AGL valid at 0030UTC and 0100 UTC on 26 May 2016 for (a-b) NoDA, (c-d) CWP, (e-f) RAD and (g-h) RADCWP experiments.

4.4 Forecast Verification

4.4.1 Characteristics of the Forecasts

The observed and predicted composite reflectivity fields are plotted in Fig. 25. They clearly demonstrate the positive impact of simultaneous using radar and CWP on the 1 hour forecast when compared to the observations (Fig25. q-t vs a-d). The forecasts in the NoDA experiment maintains the cluster of storm cells which are not supported by the observations. The major supercell near the central of the domain is completely missed (Fig.25 e-h vs a-d). While it is apparent that the forecast of reflectivity is more spatially consistent with the radar observations, deficiencies are still notable if only CWP or radar data is assimilated. In the CWP experiment, the scope of precipitation area is in more agreement with that in the observations (Fig.25 i-l vs a-d), but the area with high reflectivity values (> 60dBZ) is much bigger than that in the observations. In the RAD experiment, the area with high reflectivity is shrunk and the location of the supercell closer to the observed one, but the scope of light precipitation is too small and several spurious cells around the major storm exist. When both radar data and CWP data are assimilated in the experiment RADCWP, the forecast for major supercell is the best one among all experiments, though the area for the light precipitation is still smaller than that of the observations. The predicted intensity and location of the supercell storm is well supported by the observations during the 1 hour forecast (Fig.25 q-t). Especially, the movement of the supercell agrees well with the tornado track reported by NOAA Storm Prediction Center.

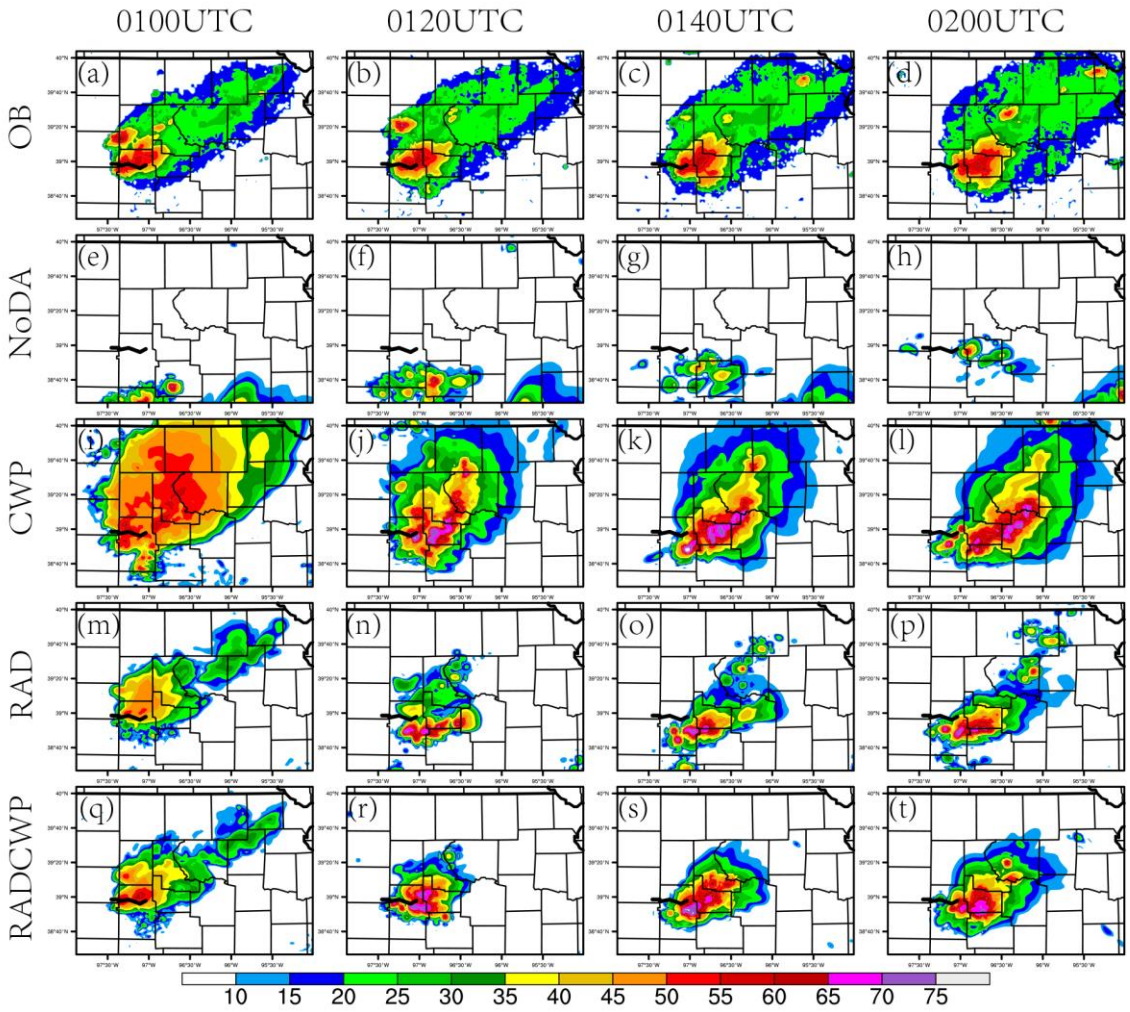

Figure 25. Observed composite reflectivity (a-d) remapped to the model grid and corresponding forecasts from (e-h) NoDA, (i-l) CWP, (m-p) RAD and (q-t) RADCWP experiments. The black line indicates the tornado track reported by NOAA Storm Prediction Center (SPC).

4.4.2 Conventional Verification

Similar to the verification procedure for idealized case, the mean biases, RMS errors are calculated and plotted for reflectivity to understand the impact of radar and CWP data on convective NWP. But the statistics for the three-dimensional wind field and temperature field are not involved here due to the lack of observation network which can resolve storm structures.

Fig. 26 exhibits the variation of mean bias and RMS errors for the radar reflectivity for all experiments during the 1 hour free forecast launched from 0100UTC. It apparently indicates that all data assimilation experiments have lower bias (i.e. closer to zero) and much lower RMS errors compared to the NoDA experiment. The CWP experiment has positive biases and all other experiments have negative biases. Bias scores for all experiments do not change too much during 1 hour forecast (top panel of Fig.26). The RMS errors for RAD and RADCWP are lower at the very beginning but increase dramatically in the first 15 minutes of forecast then become steady, or even decrease a little bit since then. CWP and RAD experiments have a similarly performance in term of RMS errors in the last 45 minutes. The RMS errors in the RADCWP experiment are consistently lowest among all experiments during the whole period of the 1 hour forecast. The results again suggest that assimilating both radar and CWP data has remarkable improvement compared to assimilating only radar data or CWP data alone in this real data case.

In addition, the PODs, FARs and HSS are plotted to evaluate forecasts for all experiments. Unlike idealized case, three different reflectivity thresholds are used to determine if the experiments will over-predict or under-predict the intensity of the storm.

The skill scores based on thresholds of 30 dBZ, 40 dBZ and 50 dBZ are plotted in Fig. 27. Basically, it shows that all DA experiments conduct some improvements in forms of a higher POD, a lower FAR and a higher HSS over the NoDA experiment. It is obvious that the NoDA experiment has no skill on 1 hour forecast. The RAD experiment generates the worst POD, but produces comparable FAR to the CWP experiment. However, with the increasing of the reflectivity threshold, the POD in RAD experiment is degraded. There is no skill at all from 0110UTC to 0130UTC when the threshold is 50 dBZ. The experiments with CWP data have a relatively stable performance. The PODs are greater than 0.8 when smaller threshold is set and only slightly degraded as the reflectivity threshold goes up. But the FAR is consistently higher than 0.8 for all reflectivity thresholds and hits 0.9 for the threshold 50 dBZ. Overall, performance of CWP is better than RAD experiment when the threshold is larger than 40 dBZ, indicating that the usefulness of CWP data in storm-scale NWP. In general, the RADSAT experiment produces the best forecast skills among all four experiments.

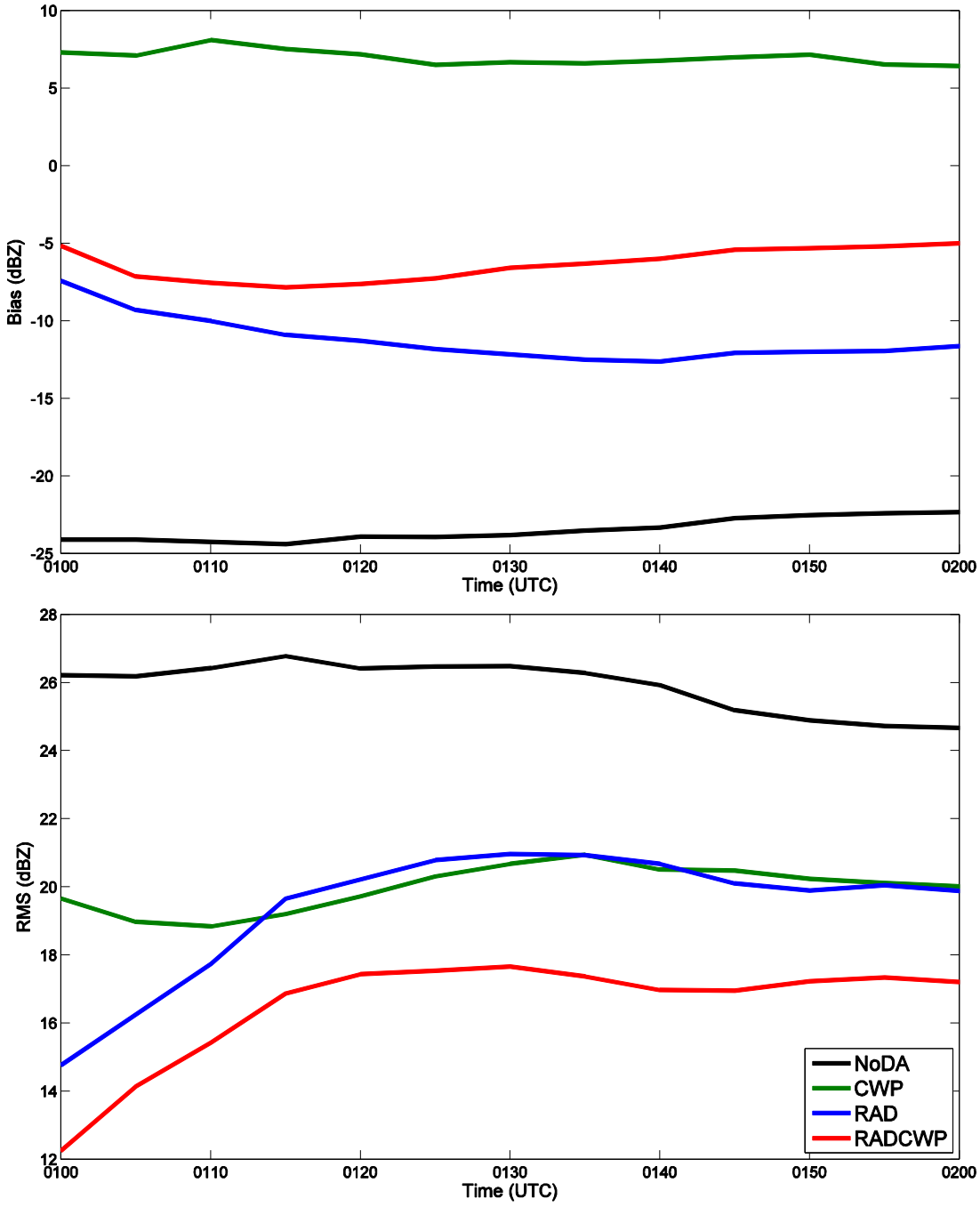

Figure 26. Mean bias (top) and RMS errors (bottom) of reflectivity over the domain d02 depicted in Fig. 20 during the 1 hour forecast initialized at 0100UTC. All experiments correspond to the Table 4.

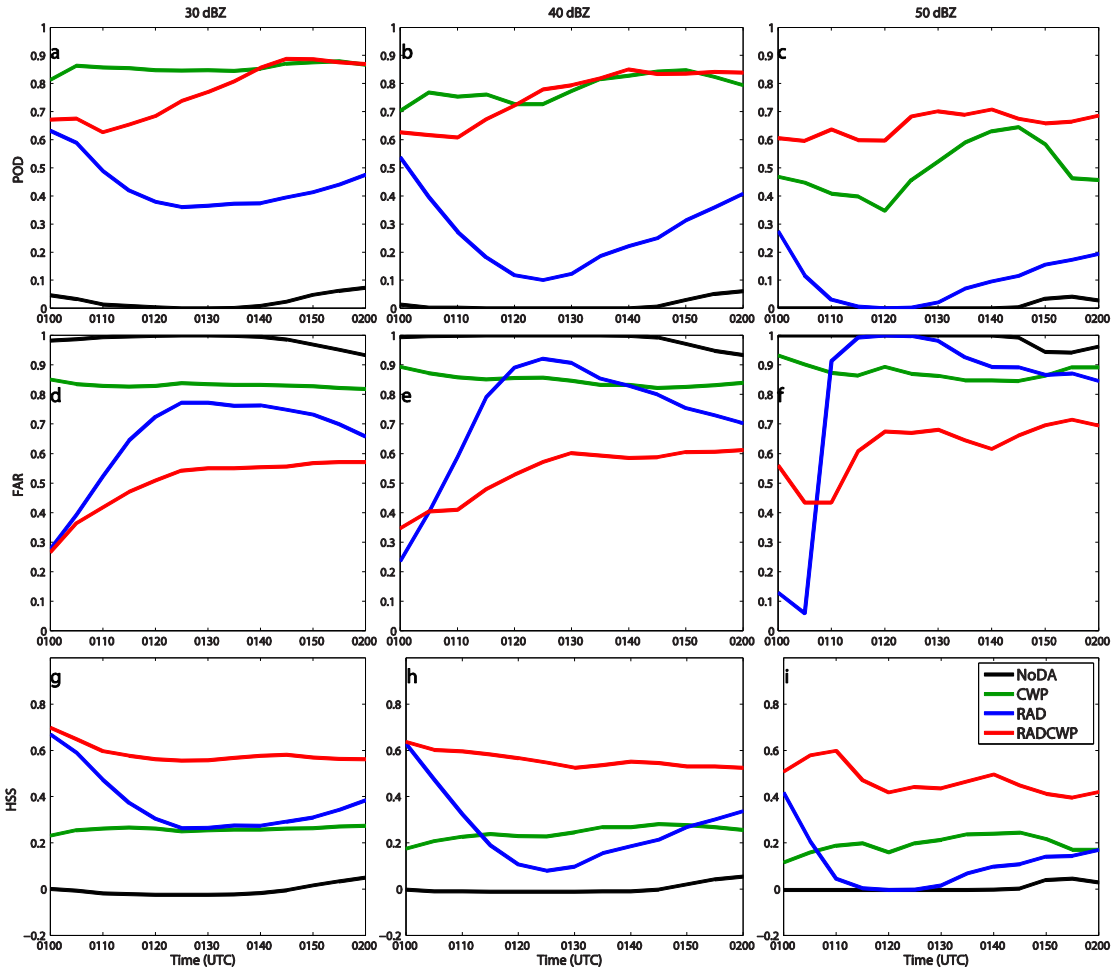

Figure 27. PODs, FARs and Heidke Skill scores for the reflectivity threshold of 30 dBZ, 40 dBZ and 50 dBZ over the domain d02. The skill scores are plotted for all experiment.

4.5 Summary

Overall, the assimilation of both radar data and satellite derived CWP data using the En3DV method can significantly improve the quality of 1 hour forecast even with limited ensemble members in this real data case. It is found that the reflectivity pattern and cold pool structure are well analyzed after 1 h data assimilation cycles. There are also some evidences that several weak spurious cells are eliminated or alleviate in the analyses by using both clear-sky CWP data as well as zero reflectivity.

The impact of assimilation of both CWP data and radar data on short-term 1 hour forecast is quite positive in this real data case, and looks much better than either radar data, or CWP data is used alone. Relatively accurate location and intensity of the supercell storm is predicted in term of the track of the storm and the best skill scores. The statistical analysis also offers the less biases and lower RMS errors for RADCWP experiments than those of other experiments. The result in this real data case along with the result in OSSEs reveals the significant benefit of utilizing both radar and CWP data to storm-scale DA and convective scale NWP.

Chapter 5 Summary and Future Work

In this study, radar radial velocity and reflectivity data, along with satellite CWP and TPW data are assimilated into WRF model using an ensemble of the En3DA system. Both an idealized case and a real data case occurred on 25-26 May 2016 are performed to investigate the impact of radar and satellite data in NWP.

In idealized case, two groups of DA and forecast experiments are performed. The first set of experiments assimilates storm-resolving radar data and CWP data under the perfect storm environment, while another group of experiments assimilate additional TPW data under the storm environment with dry biases. The advantages of simultaneously assimilating both radar and satellite data as well as importance of storm environment are shown by comparing analysis and forecast against the reference truth run.

Results from first set of experiments indicate that assimilating satellite derived CWP data is able to reduce spin-up time of convection within the model compared to only assimilating radar data. When assimilating only radar radial velocity and reflectivity data, the analysis for most directly related model variables, such as wind, is very close to the nature run, but for temperature field and non-precipitating cloud water content, which are not directly observed by radars. But satellite derived CWP data can account for this, and these data can be assimilated before precipitating clouds are generated. The RAD1 experiment underestimates the cold pool strength which is a significant characteristic of any storm, but it still produces an acceptable 1-hour forecast, though with larger biases in magnitude and location of the storms than that in RADCWP1. For the forecast in RADCWP1, the errors are actually reduced by a factor

of 2 and PODs are increased by 0.2 during the first 45-min forecast period. The combination of cloud water path and radar data produces a more accurate analysis and forecast under the perfect storm environment.

For the second group of experiments, the environment is modified to reduce the moisture content in troposphere so that the atmosphere becomes too stable to trigger and sustain convection. Assimilating only radar data does not generate sustained convection since radar data contain little information about atmospheric moisture. Much better analyses and forecasts are produced by also assimilating CWP data in RADCWP2 experiment. The right-splitting storm is able to exist much longer, up to 45 minutes in forecast, but still has a bias to the northeast of the reference truth. In addition, the left-moving storm is still not analyzed. This is because the CWP data contain cloud information, but not water vapor. It may help correct the dry bias in the storm environment but not in a dramatic way. Some positive impacts of assimilating TPW are observed in both analysis and forecast because TPW data contain the information of moisture in troposphere. Although some spurious cells develop during the process of DA, the analysis of two storms is more accurately depicted in magnitude and location by the end of the DA period. Higher POD and HSS skill scores than the other experiments suggest that the usefulness of TPW data to correct dry bias in the storm environment in this case. However, the forecast skill scores drop quickly during the 30 min forecast. This group of experiments point out that the storm environment, especially moisture, is fundamental important to the storm development. Assimilating radar data is important because these data can resolve the internal storm structure. However, the storm environment should be corrected by assimilating other

observations, such as satellite TPW data, which may contain critical information about storm environment.

The results from real data case are quite consistent with the idealized case and Jones (2013, 2015, 2016) who used EnKF approach. The benefit of combined assimilation of radar and CWP data is further revealed by the analysis and forecast of the tornadic supercell storm event on 25-26 May 2016. In the DA results, the structures of including cold pool, wind fields and reflectivity pattern are reasonably analyzed when both radar data and CWP data are assimilated. The scope and intensity of strong precipitation area (indicated by reflectivity field) and cold pool area look more reasonable. The positive impacts of both data types are also supported by the 1 hour free forecasts after DA cycling. Biases and RMS errors are reduced as well as skill scores are significantly improved in the experiment when both data are used.

Although some encouraging results are obtained in this study, many unknowns still exist. Further systematic investigation of assimilating satellite data together with radar data is necessary, especially on the topics of the sensitivities of the storm-scale NWP to different combinations of static covariance and ensemble derived covariance to the storm-scale NWP. With the availability of GOES-16 products, research is on-going for taking new data from the GOES-16 ABI. It is expected that the high- temporal and spatial resolution satellite data from new instrument will be helpful to construct both internal storm structures as well as storm environment so that convective scale NWP can be significantly improved in the future.

References

Adlerman, E. J., and K. K. Droegemeier, 2002: The sensitivity of numerically simulated cyclic mesocyclogenesis to variations in model physical and computational parameters. Mon Weather Rev, 130, 2671-2691.

Aksoy, A., D. C. Dowell, and C. Snyder, 2009: A Multicase Comparative Assessment of the Ensemble Kalman Filter for Assimilation of Radar Observations. Part I: Storm-Scale Analyses. Mon Weather Rev, 137, 1805-1824.

Anderson, J., T. Hoar, K. Raeder, H. Liu, N. Collins, R. Torn, and A. Avellano, 2009: THE DATA ASSIMILATION RESEARCH TESTBED A Community Facility. B Am Meteorol Soc, 90, 1283-1296.

Berre, L., O. Pannekoucke, G. Desroziers, S. Stefanescu, B. Chapnik, and L. Raynaud, 2007: A variational assimilation ensemble and the spatial filtering of its error covariances: increase of sample size by local spatial averaging. Proc. ECMWF Workshop on Flow-Dependent Aspects of Data Assimilation, 151-168.

Bonavita, M., L. Isaksen, and E. Holm, 2012: On the use of EDA background error variances in the ECMWF 4D-Var. Q J Roy Meteor Soc, 138, 1540-1559.

Brewster, K., M. Hu, M. Xue, and J. Gao, 2005: Efficient assimilation of radar data at high resolution for short range numericalweather prediction. World Weather Research Program Symp. and Nowcasting and Very Short-Range Forecasting WSN05, Toulouse, France, WMO World Weather Research Programme, Symp. CD, Paper 3.06.

Buehner, M., 2005: Ensemble-derived stationary and flow-dependent background-error covariances: Evaluation in a quasi-operational NWP setting. Q J Roy Meteor Soc, 131, 1013-1043.

Chen, Y. D., and Coauthors, 2015: Variational Assimilation of Cloud Liquid/Ice Water Path and Its Impact on NWP. J Appl Meteorol Clim, 54, 1809-1825.

Courtier, P., 1997: Dual formulation of four-dimensional variational assimilation. Q J Roy Meteor Soc, 123, 2449-2461.

Crum, T. D., R. L. Alberty, and D. W. Burgess, 1993: Recording, Archiving, and Using Wsr-88d Data. B Am Meteorol Soc, 74, 645-653.

Derber, J., and A. Rosati, 1989: A Global Oceanic Data Assimilation System. J Phys Oceanogr, 19, 1333-1347.

Derber, J. C., and W. S. Wu, 1998: The use of TOVS cloud-cleared radiances in the NCEP SSI analysis system. Mon Weather Rev, 126, 2287-2299.

Dowell, D. C., L. J. Wicker, and C. Snyder, 2011: Ensemble Kalman Filter Assimilation of Radar Observations of the 8 May 2003 Oklahoma City Supercell: Influences of Reflectivity Observations on Storm-Scale Analyses. Mon Weather Rev, 139, 272-294.

Dowell, D. C., F. Q. Zhang, L. J. Wicker, C. Snyder, and N. A. Crook, 2004: Wind and temperature retrievals in the 17 May 1981 Arcadia, Oklahoma, supercell: Ensemble Kalman filter experiments. Mon Weather Rev, 132, 1982-2005.

Ferrier, B. S., 1994: A Double-Moment Multiple-Phase 4-Class Bulk Ice Scheme .1. Description. J Atmos Sci, 51, 249-280.

Fierro, A. O., J. Gao, C. L. Ziegler, K. M. Calhoun, E. R. Mansell, and D. R. MacGorman, 2016: Assimilation of Flash Extent Data in the Variational Framework at Convection-Allowing Scales: Proof-of-Concept and Evaluation for the Short-Term Forecast of the 24 May 2011 Tornado Outbreak. Mon Weather Rev, 144, 4373-4393.

Gao, J. D., and D. J. Stensrud, 2012: Assimilation of Reflectivity Data in a Convective-Scale, Cycled 3DVAR Framework with Hydrometeor Classification. J Atmos Sci, 69, 1054-1065.

——, 2014: Some Observing System Simulation Experiments with a Hybrid 3DEnVAR System for Storm-Scale Radar Data Assimilation. Mon Weather Rev, 142, 3326-3346.

Gao, J. D., M. Xue, K. Brewster, and K. K. Droegemeier, 2004: A three-dimensional variational data analysis method with recursive filter for Doppler radars. J Atmos Ocean Tech, 21, 457-469.

Gao, J. D., C. H. Fu, D. J. Stensrud, and J. S. Kain, 2016: OSSEs for an Ensemble 3DVAR Data Assimilation System with Radar Observations of Convective Storms. J Atmos Sci, 73, 2403-2426.

Gao, J. D., and Coauthors, 2013: A Real-Time Weather-Adaptive 3DVAR Analysis System for Severe Weather Detections and Warnings. Weather Forecast, 28, 727-745.

Harris, B. A., and G. Kelly, 2001: A satellite radiance-bias correction scheme for data assimilation. Q J Roy Meteor Soc, 127, 1453-1468.

Houtekamer, P. L., and H. L. Mitchell, 1998: Data assimilation using an ensemble Kalman filter technique. Mon Weather Rev, 126, 796-811.

Johnson, A., and X. G. Wang, 2016: A Study of Multiscale Initial Condition Perturbation Methods for Convection-Permitting Ensemble Forecasts. Mon Weather

Rev, 144, 2579-2604.

Johnson, A., X. G. Wang, J. R. Carley, L. J. Wicker, and C. Karstens, 2015: A Comparison of Multiscale GSI-Based EnKF and 3DVar Data Assimilation Using Radar and Conventional Observations for Midlatitude Convective-Scale Precipitation Forecasts. Mon Weather Rev, 143, 3087-3108.

Jones, T. A., and D. J. Stensrud, 2012: Assimilating AIRS Temperature and Mixing Ratio Profiles Using an Ensemble Kalman Filter Approach for Convective-Scale Forecasts. Weather Forecast, 27, 541-564.

Jones, T. A., D. J. Stensrud, P. Minnis, and R. Palikonda, 2013: Evaluation of a Forward Operator to Assimilate Cloud Water Path into WRF-DART. Mon Weather Rev, 141, 2272-2289.

Jones, T. A., D. Stensrud, L. Wicker, P. Minnis, and R. Palikonda, 2015: Simultaneous Radar and Satellite Data Storm-Scale Assimilation Using an Ensemble Kalman Filter Approach for 24 May 2011. Mon Weather Rev, 143, 165-194.

Jones, T. A., K. Knopfmeier, D. Wheatley, G. Creager, P. Minnis, and R. Palikonda, 2016: Storm-Scale Data Assimilation and Ensemble Forecasting with the NSSL Experimental Warn-on-Forecast System. Part II: Combined Radar and Satellite Data Experiments. Weather Forecast, 31, 297-327.

Kuo, Y. H., X. Zou, and Y. R. Guo, 1996: Variational assimilation of precipitable water using a nonhydrostatic mesoscale adjoint model .1. Moisture retrieval and sensitivity experiments. Mon Weather Rev, 124, 122-147.

Li, J., T. J. Schmit, X. Jin, and G. Martin, 2010: GOES-R Advanced Baseline Imager (ABI) algorithm theoretical basis document for legacy atmospheric moisture profile, legacy atmospheric temperature profile, total precipitable water, and derived atmospheric stability indices. US Department of Commerce, National Oceanic and Atmospheric Administration, National Environmental Satellite, Data, and Information Service.

Lorenc, A. C., 2003: The potential of the ensemble Kalman filter for NWP - a comparison with 4D-Var. Q J Roy Meteor Soc, 129, 3183-3203.

Matricardi, M., F. Chevallier, G. Kelly, and J. N. Thepaut, 2004: An improved general fast radiative transfer model for the assimilation of radiance observations. Q J Roy Meteor Soc, 130, 153-173.

Migliorini, S., 2012: On the Equivalence between Radiance and Retrieval Assimilation. Mon Weather Rev, 140, 258-265.

Minnis, P., and Coauthors, 2008a: Cloud Detection in Nonpolar Regions for CERES

Using TRMM VIRS and Terra and Aqua MODIS Data. Ieee T Geosci Remote, 46, 3857-3884.

Minnis, P., and Coauthors, 2008b: Near-real time cloud retrievals from operational and research meteorological satellites. 710703-710703-710708.

Minnis, P., and Coauthors, 2011: CERES Edition-2 Cloud Property Retrievals Using TRMM VIRS and Terra and Aqua MODIS Data-Part I: Algorithms. Ieee T Geosci Remote, 49, 4374-4400.

Noda, A., and H. Niino, 2003: Critical grid size for simulating convective storms: A case study of the Del City supercell storm. Geophys Res Lett, 30.

Okamoto, K., A. P. McNally, and W. Bell, 2014: Progress towards the assimilation of all-sky infrared radiances: an evaluation of cloud effects. Q J Roy Meteor Soc, 140, 1603-1614.

Pavelin, E. G., S. J. English, and J. R. Eyre, 2008: The assimilation of cloud-affected infrared satellite radiances for numerical weather prediction. Q J Roy Meteor Soc, 134, 737-749.

Polkinghorne, R., and T. Vukicevic, 2011: Data Assimilation of Cloud-Affected Radiances in a Cloud-Resolving Model. Mon Weather Rev, 139, 755-773.

Polkinghorne, R., T. Vukicevic, and K. F. Evans, 2010: Validation of Cloud-Resolving Model Background Data for Cloud Data Assimilation. Mon Weather Rev, 138, 781-795.

Prates, C., S. Migliorini, S. English, and E. Pavelin, 2014: Assimilation of satellite infrared sounding measurements in the presence of heterogeneous cloud fields. Q J Roy Meteor Soc, 140, 2062-2077.

Rotunno, R., and J. Klemp, 1985: On the Rotation and Propagation of Simulated Supercell Thunderstorms. J Atmos Sci, 42, 271-292.

Saunders, R., M. Matricardi, and P. Brunel, 1999: An improved fast radiative transfer model for assimilation of satellite radiance observations. Q J Roy Meteor Soc, 125, 1407-1425.

Smith, P. L., C. G. Myers, and H. D. Orville, 1975: Radar Reflectivity Factor Calculations in Numerical Cloud Models Using Bulk Parameterization of Precipitation. J Appl Meteorol, 14, 1156-1165.

Stengel, M., M. Lindskog, P. Unden, and N. Gustafsson, 2013: The impact of cloud-affected IR radiances on forecast accuracy of a limited-area NWP model. Q J Roy Meteor Soc, 139, 2081-2096.

Stensrud, D. J., and J. D. Gao, 2010: Importance of Horizontally Inhomogeneous Environmental Initial Conditions to Ensemble Storm-Scale Radar Data Assimilation and Very Short-Range Forecasts. Mon Weather Rev, 138, 1250-1272.

Stensrud, D. J., and Coauthors, 2009: CONVECTIVE-SCALE WARN-ON-FORECAST SYSTEM A Vision for 2020. B Am Meteorol Soc, 90, 1487-+.

Sun, J. Z., 2005: Initialization and numerical forecasting of a supercell storm observed during STEPS. Mon Weather Rev, 133, 793-813.

Vukicevic, T., M. Sengupta, A. S. Jones, and T. Vonder Haar, 2006: Cloud-resolving satellite data assimilation: Information content of IR window observations and uncertainties in estimation. J Atmos Sci, 63, 901-919.

Vukicevic, T., T. Greenwald, M. Zupanski, D. Zupanski, T. Vonder Haar, and A. S. Jones, 2004: Mesoscale cloud state estimation from visible and infrared satellite radiances. Mon Weather Rev, 132, 3066-3077.

Wang, X. G., 2010: Incorporating Ensemble Covariance in the Gridpoint Statistical Interpolation Variational Minimization: A Mathematical Framework. Mon Weather Rev, 138, 2990-2995.

Wang, X. G., D. M. Barker, C. Snyder, and T. M. Hamill, 2008: A Hybrid ETKF-3DVAR Data Assimilation Scheme for the WRF Model. Part I: Observing System Simulation Experiment. Mon Weather Rev, 136, 5116-5131.

Wang, Y., and X. Wang, 2016: Direct Assimilation of Radar Reflectivity without Tangent Linear and Adjoint of the Nonlinear Observation Operator in the GSI-Based EnVar System: Methodology and Experiment with the 8 May 2003 Oklahoma City Tornadic Supercell. Mon Weather Rev.

Weisman, M. L., and J. B. Klemp, 1982: The Dependence of Numerically Simulated Convective Storms on Vertical Wind Shear and Buoyancy. Mon Weather Rev, 110, 504-520.

Weisz, E., J. Li, J. L. Li, D. K. Zhou, H. L. Huang, M. D. Goldberg, and P. Yang, 2007: Cloudy sounding and cloud-top height retrieval from AIRS alone single field-of-view radiance measurements. Geophys Res Lett, 34.

Weng, F. Z., 2007: Advances in radiative transfer modeling in support of satellite data assimilation. J Atmos Sci, 64, 3799-3807.

Weng, F. Z., and Q. H. Liu, 2003: Satellite data assimilation in numerical weather prediction models. Part I: Forward radiative transfer and Jacobian modeling in cloudy atmospheres. J Atmos Sci, 60, 2633-2646.

Wheatley, D. M., K. H. Knopfmeier, T. A. Jones, and G. J. Creager, 2015: Storm-Scale Data Assimilation and Ensemble Forecasting with the NSSL Experimental Warn-on-Forecast System. Part I: Radar Data Experiments. Weather Forecast, 30, 1795-1817.

Whitaker, J. S., and T. M. Hamill, 2012: Evaluating Methods to Account for System Errors in Ensemble Data Assimilation. Mon Weather Rev, 140, 3078-3089.

Xue, M., K. K. Droegemeier, and V. Wong, 2000: The Advanced Regional Prediction System (ARPS) - A multi-scale nonhydrostatic atmospheric simulation and prediction model. Part I: Model dynamics and verification. Meteorol Atmos Phys, 75, 161-193.

Xue, M., D. H. Wang, J. D. Gao, K. Brewster, and K. K. Droegemeier, 2003: The Advanced Regional Prediction System (ARPS), storm-scale numerical weather prediction and data assimilation. Meteorol Atmos Phys, 82, 139-170.

Xue, M., and Coauthors, 2001: The Advanced Regional Prediction System (ARPS) - A multi-scale nonhydrostatic atmospheric simulation and prediction tool. part II: Model physics and applications. Meteorol Atmos Phys, 76, 143-165.

Yussouf, N., and D. J. Stensrud, 2010: Impact of Phased-Array Radar Observations over a Short Assimilation Period: Observing System Simulation Experiments Using an Ensemble Kalman Filter. Mon Weather Rev, 138, 517-538.

Yussouf, N., E. R. Mansell, L. J. Wicker, D. M. Wheatley, and D. J. Stensrud, 2013: The Ensemble Kalman Filter Analyses and Forecasts of the 8 May 2003 Oklahoma City Tornadic Supercell Storm Using Single- and Double-Moment Microphysics Schemes. Mon Weather Rev, 141, 3388-3412.

Zhang, F. Q., C. Snyder, and J. Z. Sun, 2004: Impacts of initial estimate and observation availability on convective-scale data assimilation with an ensemble Kalman filter. Mon Weather Rev, 132, 1238-1253.

Zupanski, D., S. Q. Zhang, M. Zupanski, A. Y. Hou, and S. H. Cheung, 2011: A Prototype WRF-Based Ensemble Data Assimilation System for Dynamically Downscaling Satellite Precipitation Observations. J Hydrometeorol, 12, 118-134.